

DTIC FILE COPY

2

NAVAL POSTGRADUATE SCHOOL Monterey, California

AD-A200 944



THESIS

BACKGROUND GAS PRESSURE DEPENDENCE
OF UNIPOLAR ARCING
ON SODA LIME GLASS AND PLASTIC
INDUCED BY A CO₂ PULSED LASER

by

Adam Randall Wojtowich

June 1988

Thesis Advisor

F. Schwirzke

Approved for public release; distribution is unlimited.

DTIC
ELECTE
DEC 06 1988
S E D
E

88 12 6 0 20

REPORT DOCUMENTATION PAGE

1a. REPORT SECURITY CLASSIFICATION UNCLASSIFIED		1b. RESTRICTIVE MARKINGS	
2a. SECURITY CLASSIFICATION AUTHORITY		3. DISTRIBUTION / AVAILABILITY OF REPORT Approved for public release; distribution is unlimited.	
2b. DECLASSIFICATION / DOWNGRADING SCHEDULE			
4. PERFORMING ORGANIZATION REPORT NUMBER(S)		5. MONITORING ORGANIZATION REPORT NUMBER(S)	
6a. NAME OF PERFORMING ORGANIZATION Naval Postgraduate School	6b. OFFICE SYMBOL (If applicable) 61	7a. NAME OF MONITORING ORGANIZATION Naval Postgraduate School	
6c. ADDRESS (City, State, and ZIP Code) Monterey, California 93943-5000		7b. ADDRESS (City, State, and ZIP Code) Monterey, California 93943-5000	
8a. NAME OF FUNDING / SPONSORING ORGANIZATION	8b. OFFICE SYMBOL (If applicable)	9. PROCUREMENT INSTRUMENT IDENTIFICATION NUMBER	
8c. ADDRESS (City, State, and ZIP Code)		10. SOURCE OF FUNDING NUMBERS	
		PROGRAM ELEMENT NO.	PROJECT NO.
		TASK NO.	WORK UNIT ACCESSION NO.
11. TITLE (Include Security Classification) BACKGROUND GAS PRESSURE DEPENDENCE OF UNIPOLAR ARCING ON SODA LIME GLASS AND PLASTIC INDUCED BY A CO ₂ PULSED LASER			
12. PERSONAL AUTHOR(S) WOJTOWICH, ADAM R.			
13a. TYPE OF REPORT MASTER THESIS	13b. TIME COVERED FROM _____ TO _____	14. DATE OF REPORT (Year, Month, Day) 1988 June	15. PAGE COUNT 131
16. SUPPLEMENTARY NOTATION The views expressed in this thesis are those of the author and do not reflect the official policy or position of the Department of Defense or the U.S. Government.			
17. COSATI CODES		18. SUBJECT TERMS (Continue on reverse if necessary and identify by block number)	
FIELD	GROUP	SUB-GROUP	
		CO ₂ Pulsed Laser, Unipolar Arcing, Plasma effects, Laser Pitting, Laser Damage to Glass and Plastic.	
19. ABSTRACT (Continue on reverse if necessary and identify by block number) <i>approx 52500000 sq cm. carbond</i> An experiment was conducted to determine the background gas pressure dependence of laser induced unipolar arcing (UA) on soda lime glass and polystyrene (plastic). A CO ₂ pulsed laser was used to produce a power density of 5.25×10^9 W/cm ² , and the background pressure was varied from 1.0 atmosphere (atm) to 10^{-8} atm (10^{-8} torr). <i>10 to the 8th - 8th</i> For glass at 1.0 atm, the UA crater density at the damaged area's center was maximum and between 1.0 and 0.1 atm, it decreased linearly as the pressure dropped. UA did not occur outside of the heavily damaged area. Between 0.1 and 0.001 atm, UA occurred outside the heavily damaged area and both the center and perimeter crater density remained constant. A wave-like ring burn pattern was observed showing the influence of plasma dynamics on the laser beam propagation. Below 0.001 atm, the UA increased at the perimeter and target center, and peaked at approximately 0.0005 atm. The crater density remained constant for lower pressures. A proposed model for this interaction is outlined. <i>laser damage, the</i> Damage at the plastic target's center was too intense for analysis, but UA outside the			
20. DISTRIBUTION / AVAILABILITY OF ABSTRACT <input checked="" type="checkbox"/> UNCLASSIFIED/UNLIMITED <input type="checkbox"/> SAME AS RPT. <input type="checkbox"/> DTIC USERS		21. ABSTRACT SECURITY CLASSIFICATION UNCLASSIFIED	
22a. NAME OF RESPONSIBLE INDIVIDUAL F. Schwirzke		22b. TELEPHONE (Include Area Code) (408) 646-2635	22c. OFFICE SYMBOL 61Sw

[19] intensely damaged area occurred at 0.15 atm and increased to a maximum at 0.0005 atm.
UA remained constant below 0.0005 atm.

Accession For	
NTIS GRA&I	<input checked="" type="checkbox"/>
DTIC TAB	<input type="checkbox"/>
Unannounced	<input type="checkbox"/>
Justification	
By _____	
Distribution/	
Availability Codes	
Dist	Avail and/or Special
A-1	



Approved for public release; distribution is unlimited.

Background Gas Pressure Dependence
of Unipolar Arcing
on Soda Lime Glass and Plastic
Induced by a CO₂ Pulsed Laser

by

Adam R. Wojtowich
Captain, United States Army
B.S. Physics, DePaul University, 1979

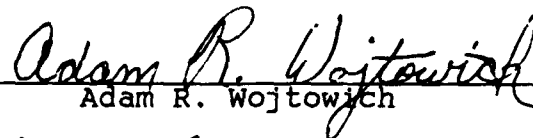
Submitted in partial fulfillment of the
requirements for the degree of

MASTER OF SCIENCE IN ENGINEERING SCIENCE

from the

NAVAL POSTGRADUATE SCHOOL
June 1988

Author:


Adam R. Wojtowich

Approved by:



F. Schwirzke, Thesis Advisor



K. E. Woehler, Second Reader



K. E. Woehler, Chairman,
Department of Physics



Gordon E. Schacher,
Dean of Science and Engineering

ABSTRACT

An experiment was conducted to determine the background gas pressure dependence of laser-induced unipolar arcing (UA) on soda lime glass and polystyrene (plastic). A CO₂ pulsed laser was used to produce a power density of 5.25×10^6 W/cm², and the background pressure was varied from 1.0 atmosphere (atm) to 10^{-8} atm ($\sim 10^{-6}$ torr).

For glass at 1.0 atm, the UA crater density at the damaged area's center was maximum and between 1.0 and 0.1 atm, it decreased linearly as the pressure dropped. UA did not occur outside of the heavily damaged area. Between 0.1 and 0.001 atm, UA occurred outside the heavily damaged area and both the center and perimeter crater density remained constant. A wave-like ring burn pattern was observed showing the influence of plasma dynamics on the laser beam propagation. Below 0.001 atm, the UA increased at the perimeter and target center, and peaked at approximately 0.0005 atm. The crater density remained constant for lower pressures. A proposed model for this interaction is outlined.

Damage at the plastic target's center was too intense for analysis, but UA outside the intensely damaged area occurred at 0.15 atm and increased to a maximum at 0.0005 atm. UA remained constant below 0.0005 atm.

TABLE OF CONTENTS

I.	INTRODUCTION -----	1
II.	BACKGROUND AND THEORY -----	3
	A. INTRODUCTION -----	3
	B. LASER-TARGET INTERACTIONS -----	3
	C. SCHWIRZKE UNIPOLAR ARCING MODEL -----	8
III.	EXPERIMENTAL EQUIPMENT AND RESEARCH TECHNIQUES --	13
	A. INTRODUCTION -----	13
	B. EXPERIMENTAL APPARATUS -----	13
	C. EXPERIMENTAL PROCEDURES -----	26
	D. EXPERIMENTAL ERRORS AND LIMITATIONS -----	29
IV.	EXPERIMENTAL RESULTS -----	33
	A. INTRODUCTION -----	33
	B. GLASS (SODA LIME) TARGETS -----	33
	C. PLASTIC (POLYSTYRENE) TARGETS -----	72
V.	ANALYSIS OF DATA -----	82
	A. INTRODUCTION -----	82
	B. GLASS TARGET ANALYSIS -----	82
	C. PLASTIC TARGET ANALYSIS -----	91
	D. LASER-GLASS INTERACTION MODEL (LGI) -----	95
VI.	CONCLUSIONS AND RECOMMENDATIONS -----	100
APPENDIX A: LUMONICS TE-822HP CO ₂ LASER OPERATING		
	PROCEDURE -----	103

APPENDIX B: VEECO 400 VACUUM SYSTEM OPERATING

PROCEDURES -----	113
LIST OF REFERENCES -----	120
INITIAL DISTRIBUTION LIST -----	122

ACKNOWLEDGMENTS

I wish to thank Mr. Robert Sanders and Mr. Thomas Kellogg for their many hours of assistance in the operation of the equipment in the Physics Department and the Material Science Department.

Mr. George Jaksha and Mr. Steve Blankschein provided crucial support in the fabrication of specific equipment necessary for this investigation.

Professor Schwirzke's assistance and guidance, combined with his expertise, have made this project a very exciting and rewarding experience. I appreciated all of his support.

Throughout this thesis, Professor Woehler's advice has been sincerely appreciated. The review and constructive comments were greatly appreciated.

Finally, I sincerely want to thank my wife, [REDACTED] whose support, understanding, patience, and encouragement made this endeavor possible.

I. INTRODUCTION

Several important Defense Department programs are utilizing high power lasers for weapons of the future [Ref. 1]. In order for these lasers, which are being further developed, to reach their fullest potential, a thorough understanding of the laser-target interactions is crucial. In addition this understanding will serve as a vital link to the development of laser target defensive measures for both metals and dielectric materials. This study investigates the background pressure dependence of the primary laser-damage mechanism, specially unipolar arcing. [Ref. 2]

It has been established that the three major laser-plasma-surface interactions are evaporation, sputtering, and unipolar arcing. Of these three interactions, unipolar arcing, which is an electrical plasma-surface interaction that leads to crater formation, has been recognized as the primary damage mechanism for metals. [Ref. 2] Numerous research projects have been completed at the Naval Postgraduate School; however, the research has been mainly confined to metals. In Olson's research of polished stainless steel (SS304), he observed fewer arc craters at 10^{-6} torr than at atmospheric pressure [Ref. 3]. This data indicated a decrease on the order of one-third fewer

craters per square centimeter at the lower pressure; intermediate pressures were not evaluated.

In the course of this investigations into unipolar arcing, two types of vacuum chamber windows, one of ZnSe and the other of NaCl, were damaged. Upon closer examination of the damaged areas, unipolar arcing craters were observed. This indication of a plasma formation from a nonconducting medium initiated this investigation into the background gas pressure dependence of unipolar arcing on nonconducting materials. Specifically, this study examined the background gas pressure dependence of unipolar arcing on soda lime glass and plastic using a CO₂ Lumonics TEA laser (10.6 microns) and a Veeco vacuum chamber. The glass and plastic targets were irradiated with a focused beam of power density 5.25×10^6 watts per square centimeter at different pressures ranging from atmospheric pressure to 10^{-8} atmospheres.

II. BACKGROUND AND THEORY

A. INTRODUCTION

An understanding of the laser-target interactions is essential to the understanding of the pressure dependence of unipolar arcing on glass and plastic targets. A brief summary of the significant pulsed laser-target interactions for glass targets will be presented and is based primarily on the research conducted at the Army Materials and Mechanics Research Center [Refs. 4,5]. Finally, a summary of the current model for unipolar arcing, the Schwirzke model, will be presented.

B. LASER-TARGET INTERACTIONS

When a pulsed laser beam interacts with a glass surface, the damage resulting from the deposition of laser energy is generally classified into two categories: mechanical and thermal. A third category is added to include the plasma effects. Table 2.1 depicts the major laser target interactions in each of the three categories listed above. Although these effects usually occur simultaneously, most of these effects depend on temperature and the energy output of the laser.

The three thermal effects are dependent on the heat transfer in the irradiated glass. Desorption is defined as the process by which a bond between a solid surface and the

TABLE 2.1

PULSED LASER-TARGET INTERACTIONS FOR GLASS

THERMAL EFFECTS	MECHANICAL EFFECTS	PLASMA EFFECTS
Desorption	Laser-Supported-Absorption Waves (LSA)	Desorption
Vaporization	Cracking/Exfoliation	Vaporization
Cracking/Exfoliation		Ion Sputtering
		Unipolar Arcing

adsorbed gas molecules is ruptured. This results in the removal of the gas molecules ($H_2, H_2O, O_2, etc.$) from the solid's surface and depends on the surface condition of the target, the temperature of the target, and the surrounding atmosphere. This process is driven by either thermal motion, photon induced excitation, or electron and ion collisions. [Ref. 6] Vaporization results from the process in which the target's absorption of radiant heat increases the surface temperature and the vapor pressure. It is dependent only on the absorption depth and the fluence incident on the glass target. [Ref. 7] Cracking or exfoliation is a thermal/mechanical effect. The cracking process depends on the fluence incident on the glass target, the thermal expansion coefficient, the absorption depth, and the viscosity of the glass. In reference 5, it was deduced that exfoliation occurs as a direct result of the viscoelastic stress relaxation within the skin depth of the impacted glass surface.

During the laser pulse the temperature of the glass increases and thermal expansion occurs. Because of the elevated temperature, the glass flows with decreasing viscosity. Subsequent to the cessation of the laser pulse, the temperature rapidly decreases and the glass contracts while flowing with increasing viscosity. This results in thermal stress being frozen into the material. Cracks which relieve this stress are initiated by the presence of a Griffith microcrack distribution on the surface. If the developed cracks are deep enough, they peel horizontally, providing further stress relief which results in the glass surface being covered with flakes. [Ref. 5, p.11,14]

The mechanical effects that are prevalent in high energy lasers are cracking and exfoliation as described above and the laser-supported absorption waves. There are usually two major types of these waves: laser-supported-detonation waves and laser-supported-combustion waves. The laser-supported-detonation wave, which propagates as a shock wave, moves at supersonic velocity and is normally formed at an irradiance of 10^7 to 10^9 W/cm², whereas the laser-supported-combustion wave moves at subsonic speeds and is formed at a lower irradiance of 10^3 to 10^7 W/cm². The factors governing the two moving waves are the atmospheric pressure, vaporized target material, the state of the surface, the laser wavelength and pulse width, and the laser irradiance. It was determined that the laser-supported-detonation waves propagate with a velocity V_{LSD} given by equation 2.1 where Γ = ratio of specific heats, I = laser irradiance, and ρ = gas density.

$$V_{LSD} = [2(\Gamma^2 - 1)I/\rho]^{1/3} \quad (\text{eqn. 2.1})$$

As the wave propagates towards the laser, conservation of momentum produces a pressure pulse into the target; this enhances the exfoliation. These waves are important because a large fraction of the total laser power incident on a target can be absorbed by these waves. For a complete summary of the laser-supported-absorption waves, see references 8,9, and 10.

The third category of laser-target effects is the one due to plasma effects. When a hot plasma is formed by the incident laser pulse, this produced plasma is in contact with the glass target. Both thermal and electrical interactions occur which result in the breakdown of the target surface. In addition to the two thermal effects of desorption and vaporization that were previously described, sputtering becomes a significant effect when a plasma forms. When a sufficiently energetic neutral atom or ion imparts enough energy to a wall surface atom so that it exceeds the binding energy, sputtering occurs. In addition to these thermal effects, an electrical effect occurs which results in the formation of craters on the target surface. This cratering has been called laser pitting and most recently unipolar arcing. This effect is described by the Schwirzke model for unipolar arcing. [Ref. 2]

In Figure 2.1, a flow chart of the significant events for the illumination of glass targets are mapped out.

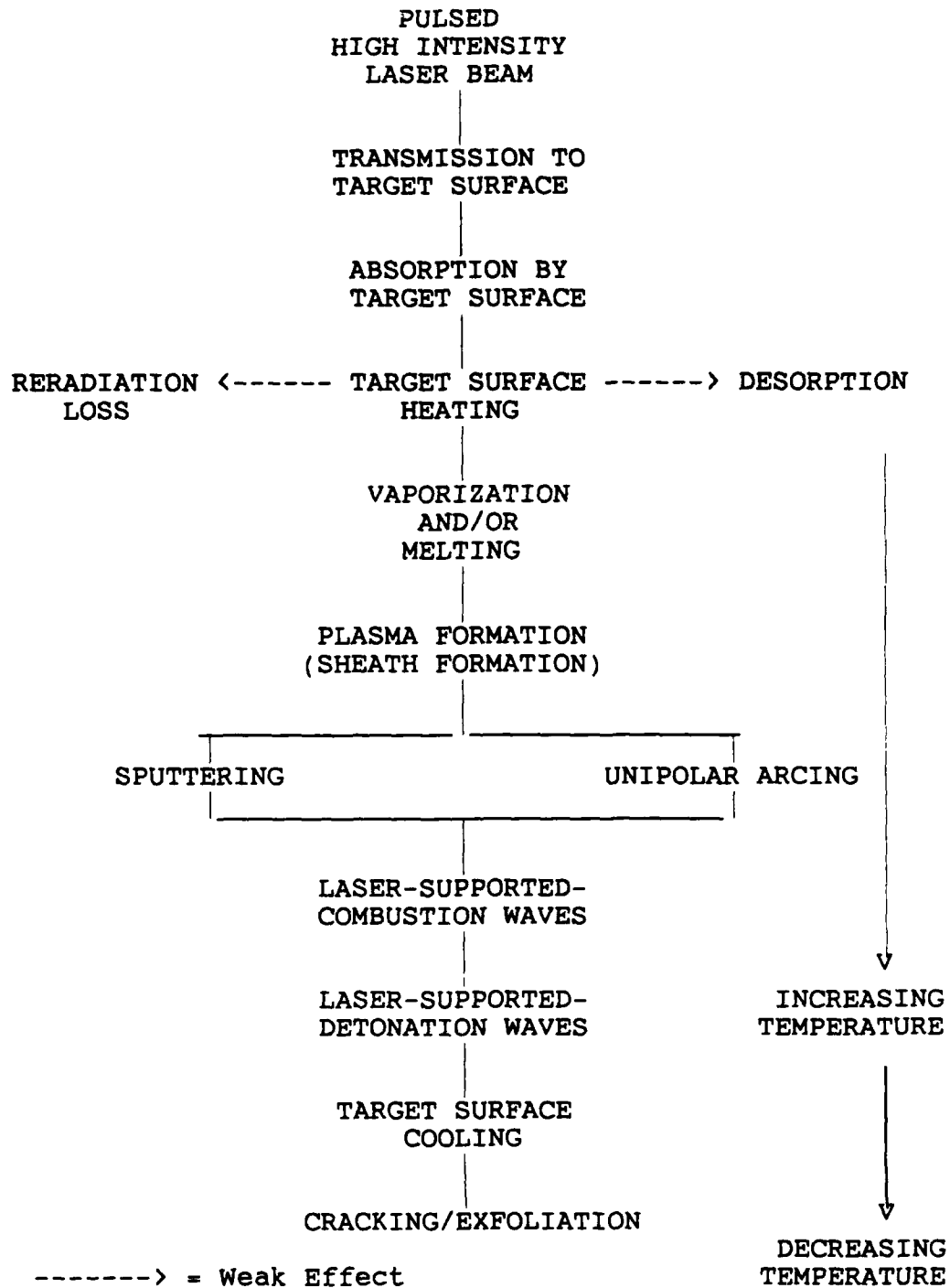


Figure 2.1 Laser Target Interaction for High Energy Lasers

C. SCHWIRZKE UNIPOLAR ARCING MODEL

1. History

In the late 1950's, A.E. Robson and P.C. Thonemann developed a model for a cathode spot on an isolated metal surface immersed in a plasma of a gas discharge. They called this phenomenon, unipolar arcing. [Ref. 11] In the early 1980's, Fred Schwirzke published a series of papers describing this same process and refining a new model for the unipolar arc [Refs. 2,12,13].

2. Model

The current model for unipolar arcing consists of a sequence of events on a time scale of nanoseconds. Many of these events occur concurrently. The following description of the unipolar arcing model is based on material presented in references 2,3,6,11,12,and 13. The sequence of events for the model are as follows:

a. Initial Laser-Target Interaction

When the laser pulse initially hits the metal target, the temperature of the target surface increases and desorption of any contaminating surface gases and water vapor occurs. (Figure 2.2)

b. Plasma Formation

There is electron heating for the initial electron density present on the surface. These energetic electrons ionize the neutral gases emitted through desorption, and a low density plasma layer is formed at the target surface.

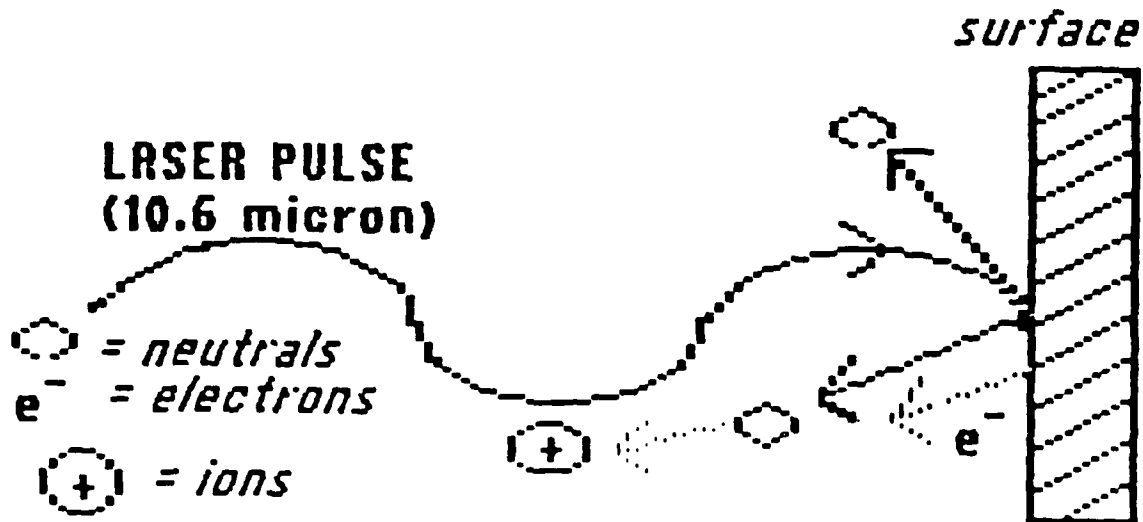


Figure 2.2 Laser-Target Interaction

c. Electric Field Formation/Sheath Formation

The lighter, more energetic electrons have higher temperatures and thermal velocities as compared to the heavier and slower ions in the plasma. The initial, increased electron flux to the target surface resulted in a net positively charged plasma. In order to maintain the plasma's quasineutrality, a plasma sheath is formed at the plasma-surface interface with a potential drop across the sheath equivalent to the floating potential (V_f), a sheath depth equal to the Debye length (λ_D), and an electric field within the sheath equal to V_f/λ_D . The floating potential and Debye length are defined in equations 2.2 and 2.3.

$$V_f = (kT_e/2e) \ln(M_i/2\pi m_e) \quad (\text{eqn. 2.2})$$

$$\lambda_D = (\epsilon_0 k T_e / n e^2)^{1/2} \quad (\text{eqn. 2.3})$$

k = Boltzmann Constant

T_e = Electron Temperature

e = Electron Charge

M_i = Ion Mass

m_e = Electron Mass

ε₀ = Free Space Permittivity

n = Plasma Density

d. Plasma Density Buildup

The plasma density will continue to increase until it reaches a critical density which occurs when the laser radian frequency equals the plasma frequency (Equation 2.4). At this critical density, the target's surface will be totally shielded from the laser pulse.

$$\omega_{\text{cutoff}} = \omega_{\text{laser}} = \omega_p = (n e^2 / \epsilon_0 m_e)^{1/2} \text{ rad/sec} \quad (\text{eqn. 2.4})$$

The electron temperature within the plasma and thus the sheath's floating potential continues to increase as the plasma absorbs more of the laser energy. As the potential increases, the more energetic ions reach the surface for recombination thereby increasing the surface temperature and the sputtering rate of neutral particles into the

plasma. This increased number of neutral particles are ionized by the higher energy electrons resulting in increased plasma density.

e. Electric Field Concentration/Arc Initiation

For the ideal target surface, the electric field lines would be normal to the target surface throughout the sheath. Crystalline imperfections, dislocations, inclusions, surface protrusions or whiskers would cause the electric field lines to converge on these imperfections thereby influencing the surface recombination process. An example of a whisker imperfection is depicted in Figure 2.3. The higher recombination rate results in an increase in the neutral particle density, ionization rate, plasma density, and the electric field. These increases will result in crater formation as depicted in Figure 2.4.

f. Arc Cessation

As the plasma density increases above the arc spot, the Debye length, i.e. sheath width, decreases and the plasma conforms to the contour of the crater. As the crater tunnels deeper, the density inside the crater increases and the electron temperature decreases resulting in the arc spot's electric field reduction. When the electric field reduces to the point that arcing can not be sustained, arc cessation occurs.

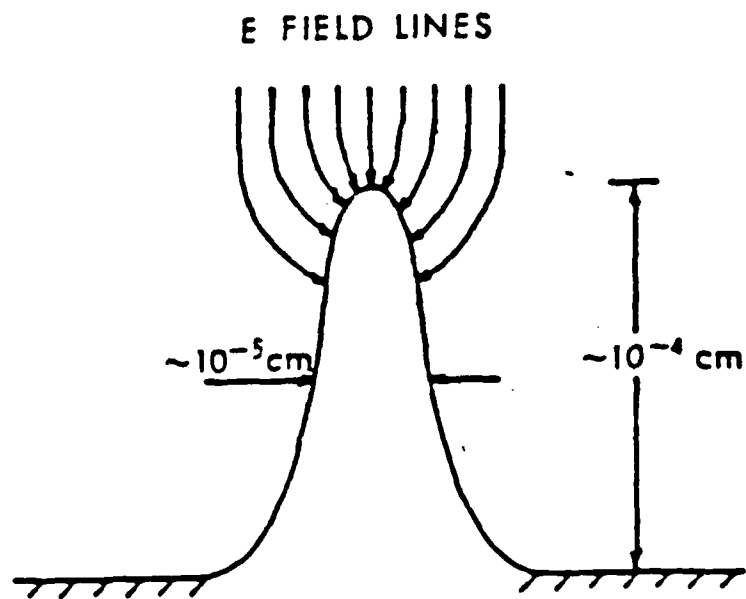


Figure 2.3 Whisker Imperfection

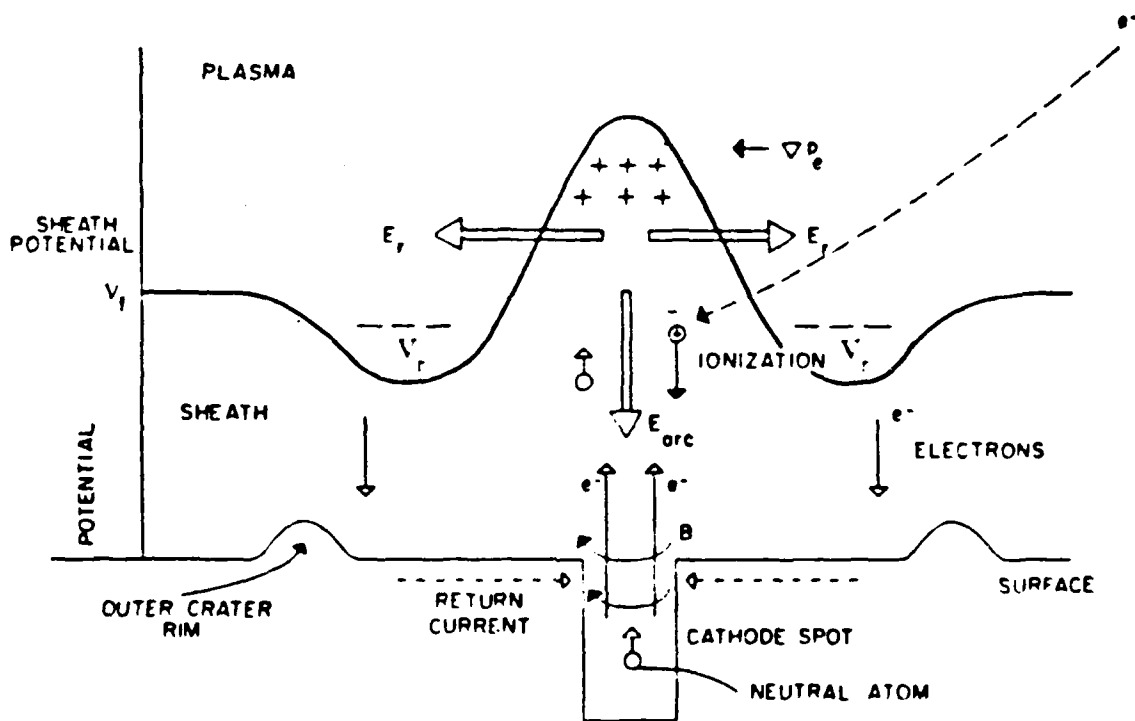


Figure 2.4 Unipolar Arcing Model

III. EXPERIMENTAL EQUIPMENT AND RESEARCH TECHNIQUES

A. INTRODUCTION

This experiment was designed to determine the pressure dependence of unipolar arcing for soda lime glass and plastic utilizing a CO₂ pulsed laser and a Veeco vacuum system. In this section, the equipment and experimental procedures are described along with their limitations and accuracy.

B. EXPERIMENTAL APPARATUS

1. Laser

The Lumonics TE-822HP CO₂ high energy TEA pulsed laser (Figure 3.1) was utilized to irradiate all targets. This laser's active medium consists of a continually

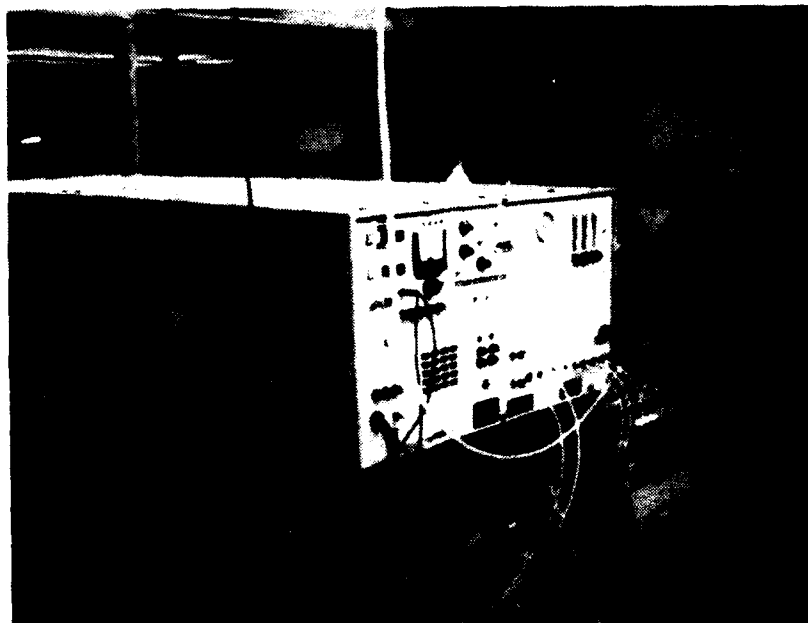


Figure 3.1 Lumonics TE-822HP CO₂ Laser

flowing gas mixture of He, N₂ and CO₂. In the single pulse mode, it is capable of delivering a maximum of 20 joules of output with an adjustable pulse width of 0.05 microseconds to 5.0 microseconds and an unfocussed burn pattern of 30mm x 33mm. In the multiple pulse mode, the laser is capable of delivering a maximum of 8 joules per pulse. The targets were illuminated with a power density of 5.25×10^6 watts/cm² and a fluence of 29.4 joules/cm². The laser's nonregulated high voltage power supplies were cooled by an external H₂O refrigeration unit and controlled by a voltage regulator. It was also necessary to control the laser cavity's temperature because of the sensitivity of the internal optics to temperature changes of ± 10 degrees Fahrenheit. [Refs. 3,6]

2. Vacuum System

The VEECO 400 vacuum system (Figure 3.2) is utilized in conjunction with the CO₂ laser for research of plasma surface interactions at the Naval Postgraduate School. The system is a modified vacuum deposition system which has been refitted with a vacuum chamber. The vacuum pumping system consists of a mechanical pump, a water cooled diffusion pump, and a liquid N₂ cooled cold trap. The pressure range of the chamber is from 1.0 atmosphere down to 10^{-9} atmospheres (atm). Three different gauges are required to determine the pressure in different ranges. Pressures from one atmosphere (760 torr) down to 0.005



Figure 3.2 Veeco 400 Vacuum System

atmosphere (3.8 torr) are measured from a Matheson pressure gauge (model 63-5601) mounted on the top of the chamber; this gauge contains a Bourdon tube and socket [Ref. 15]. Pressures between 10^{-3} atmosphere (0.76 torr) and 10^{-6} atmosphere (7.6×10^{-4} torr) are measured by a thermocouple gauge located below the chamber. Pressures between 10^{-6} atmosphere (7.6×10^{-4} torr) and 10^{-9} atmosphere (5.5×10^{-6} torr) are measured by an ionization gauge located above the diffusion pump. The vacuum chamber contains four ports with glass windows filling two of the ports, and a metal plate filling the third port. The fourth port, the laser beam entrance port, utilized two types of windows: ZnSe and NaCl.

3. Energy Meters

The laser energy output was measured by three different sets of equipment; however, only one configuration, which had been recently calibrated, proved to give reliable and consistent energy readings. A Laser Precision Corporation pyroelectric energy meter (model Rk-3230) combined with an energy probe (model RkP-336), were utilized to determine the energy output of the laser (Figure 3.3). This instrument was designed to measure the total energy content of the laser pulses with durations ranging from one millisecond down to less than a nanosecond. The wavelength range is from 0.25 to 16 microns, and the energy range is from 20 millijoules to 10

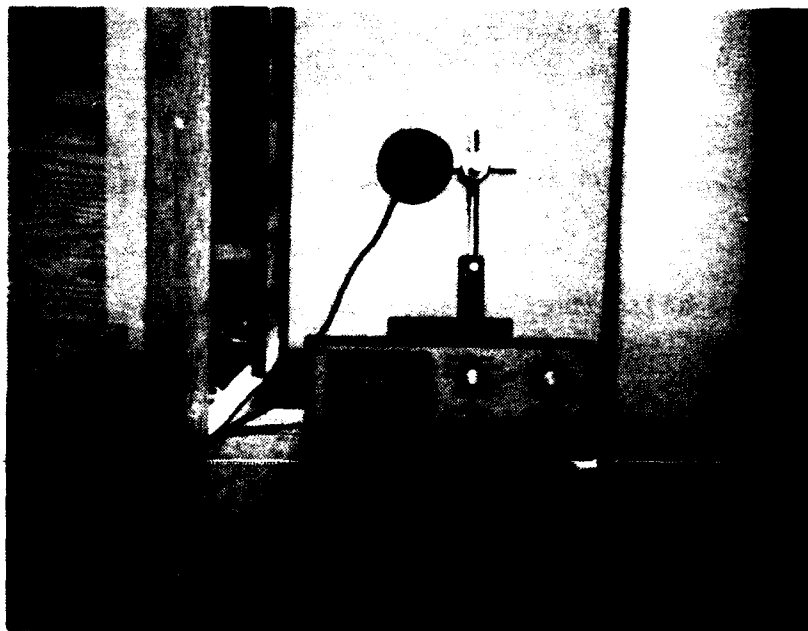
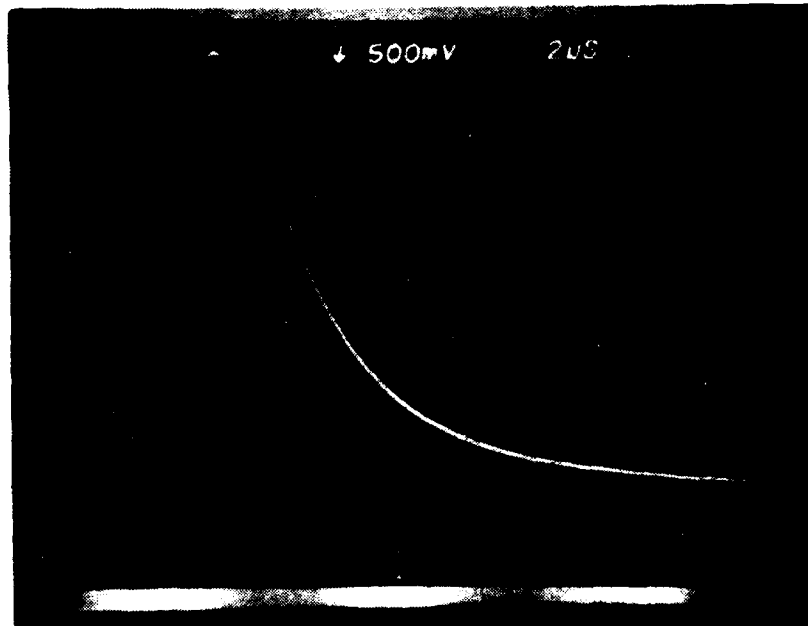


Figure 3.3 RJ-7000 Energy Meter and RJP-700 Probe

joules. The energy meter and probe (models Rj-7000 and RjP-700) gave erratic and erroneous data and they were sent in for repairs. A Hydron calorimeter verified the consistency of the laser, but due to the fact that its only calibration occurred in 1972, energy accuracy was impossible to verify. Several companies were contacted but unable to calibrate this piece of equipment.

4. Pulse Width Detector

The infrared laser pulse detector (model DMSL-12) combined with a 7904 oscilloscope, a 12 volt/80 milliamp power supply, and a C-50 series camera pack, were utilized to determine the pulse width (Figure 3.4).



Vertical Axis - approximately 500 millivolts per division

Horizontal Axis - 2 microseconds per division

Figure 3.4 CO₂ Pulse

Due to sensitivity of the liquid N₂ cooled detector, it was necessary to place a ZnSe beam splitter and a glass slide in the laser-detector beam path. The full width at half maximum (FWHM) is 5.61 microseconds with a precision of 3.63 percent; the gas flow for these measurements is described in Appendix A.

5. Optics

The following special optics, for 10.6 micron wavelength light, were utilized during this investigation:

1. One 3" diameter ZnSe beam splitter with 99.38% reflectance, 0.13% transmittance, and 0.49% absorption at 45 degrees incidence.
2. Two ZnSe 3" diameter windows with anti-reflective coatings and 96% transmittance.
3. One 3" diameter, ZnSe lens with a 14.96" focal length (F.L.), 98.5% transmittance, and 0.26% absorption.
4. One 3" diameter, 0.5m F.L., concave, copper mirror.
5. One 4" diameter flat copper mirror.
6. Two 3" diameter NaCl windows.

6. Equipment Configuration

There were two different equipment configurations used in this investigation. The first configuration (Figure 3.5) consisted of the CO₂ laser, the ZnSe beam splitter, the copper flat mirror, the copper concave mirror, the energy meter and probe, and the vacuum chamber with either the NaCl or ZnSe window. This configuration caused vacuum chamber window damage because of the

astigmatism of the concave mirror [Ref. 16]. The astigmatism increased the energy density beyond the damaging threshold of the window. The second configuration (Figure 3.6) consisted of the CO₂ laser, the ZnSe beam splitter, the ZnSe focussing lens, the energy meter and probe, and the vacuum chamber with the ZnSe window. The chamber window was located 6.9" from the focussing lens, well within the 14.96" focal length, preventing window damage. The target was held in a fixture inside the vacuum chamber (Figure 3.2) at a distance of 13.6" from the lens. This configuration produced burn patterns as depicted in Figure 3.7 and 3.8 for one atmosphere and 10⁻⁸ atmosphere of pressure respectively. In both configurations, a 35"x35"x1/4" steel plate with grid was used for optic fixture placement. As noted by Weston [Ref. 6], the laser was temperature sensitive; therefore during the experiment, the ambient temperature was maintained at 72±4 degrees Fahrenheit, and during nonoperational periods, the laser's cavity was maintained at approximately the same temperature.

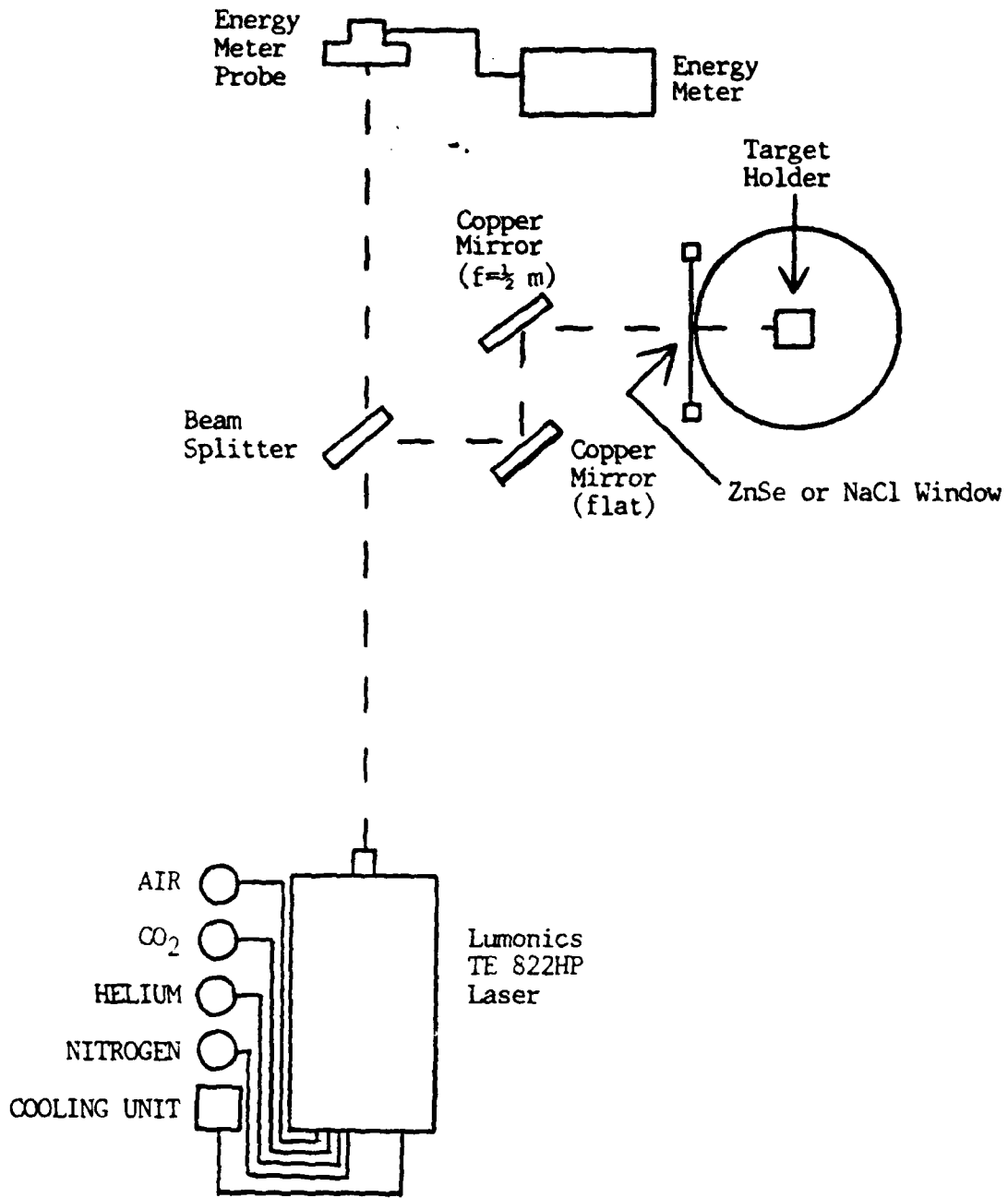


Figure 3.5 Configuration 1

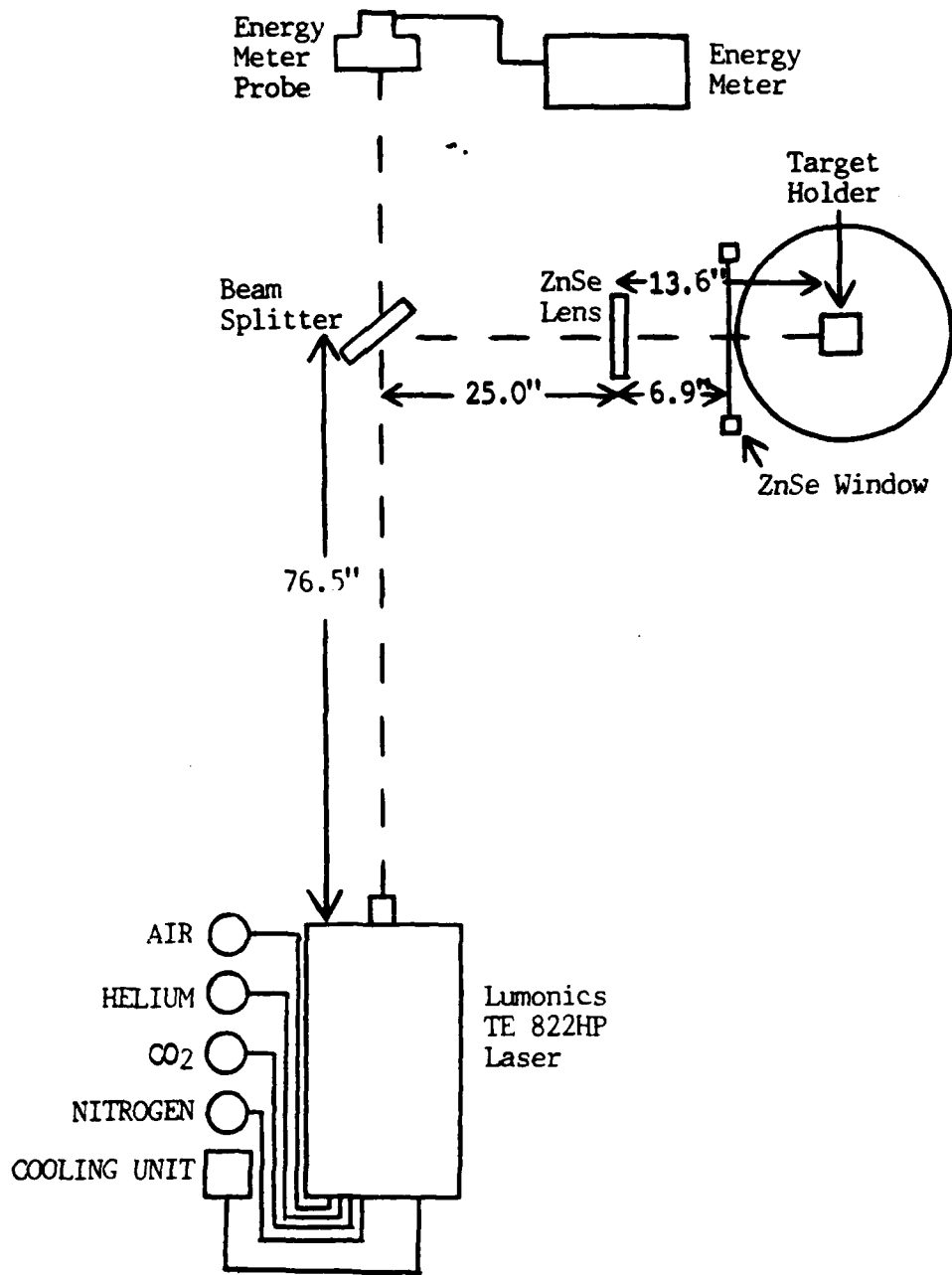


Figure 3.6 Configuration 2



Figure 3.7 Burn Pattern (10X)(Atmospheric Pressure)

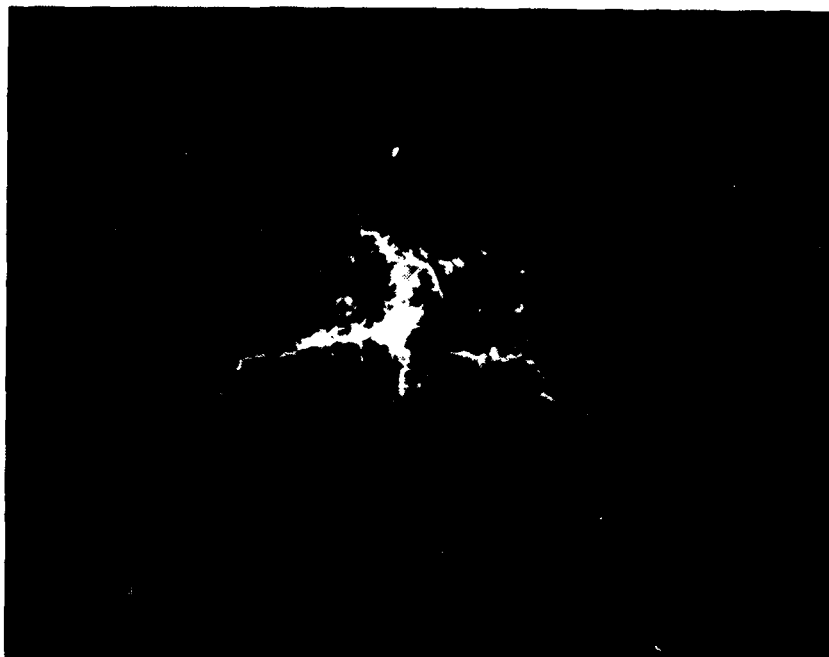


Figure 3.8 Burn Pattern (10X) (10^{-8} Atmosphere)

7. Ultra Sonic System

The Sonicor ultra sonic system (model SC-101TH) was used to clean the glass targets (Figure 3.9). Reagent and technical grade ethanol and distilled water were used in conjunction with the system to clean the glass. A blow drier was used to dry the glass after removal from the system.



Figure 3.9 Ultra Sonic System

8. Veeco Vacuum Deposition System

The Veeco automatic VS-401 vacuum deposition system (Figure 3.10) was utilized to coat the glass targets with either gold or aluminum [Ref. 17]; this allowed target examination with the scanning electron microscope.

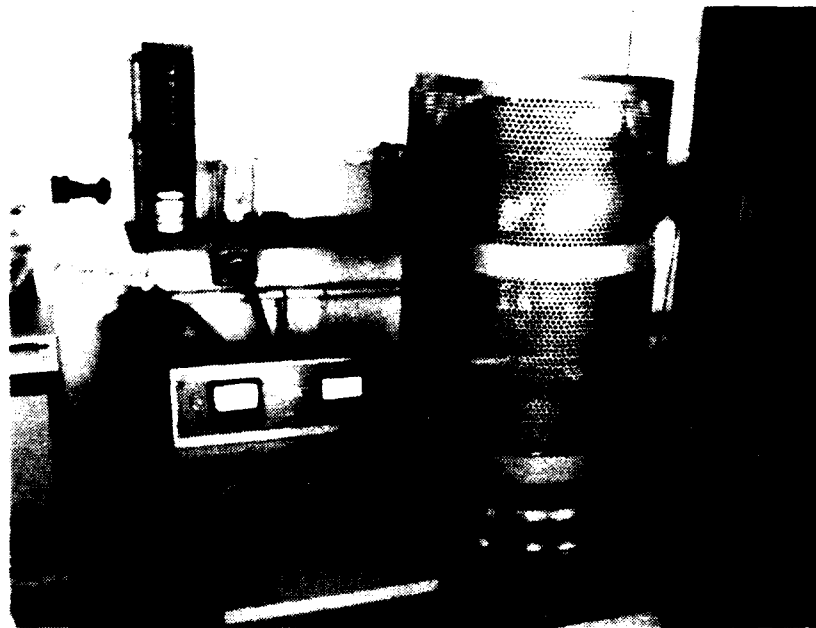


Figure 3.10 Vacuum Deposition System

9. Microscopes

The microscopes used to record and document data were primarily metallurgical, optical microscopes. For powers from 8X to 64X, a Zeiss stereomicroscope (model SV8) was utilized (Figure 3.11). For powers of 50X to 1000X, a Zeiss ICM 405 inverted camera microscope with reflecting light was utilized (Figure 3.12). The Cambridge stereoscan 200 scanning electron microscope, with magnification from 30X to 300,000X, was utilized for evaluating glass targets coated with conducting materials.

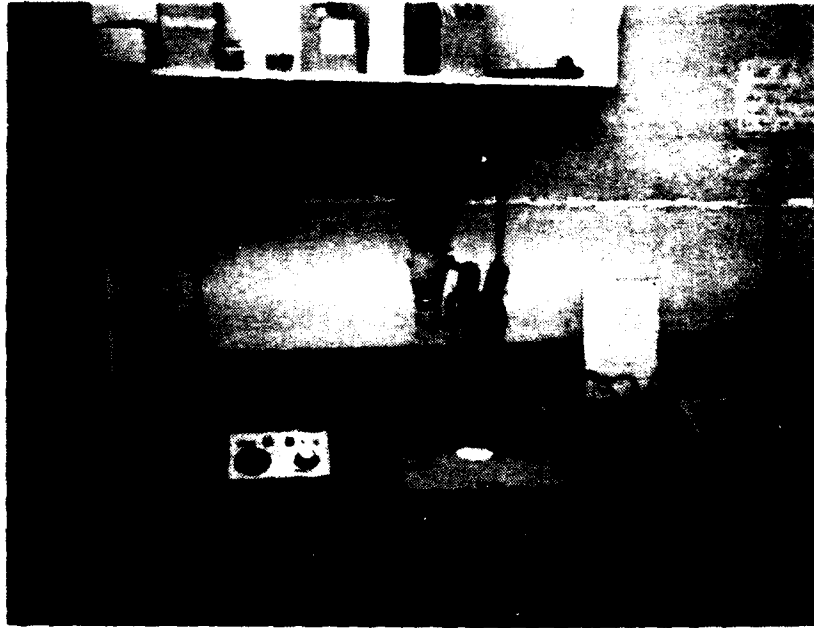


Figure 3.11 ZEISS STEREOMICROSCOPE

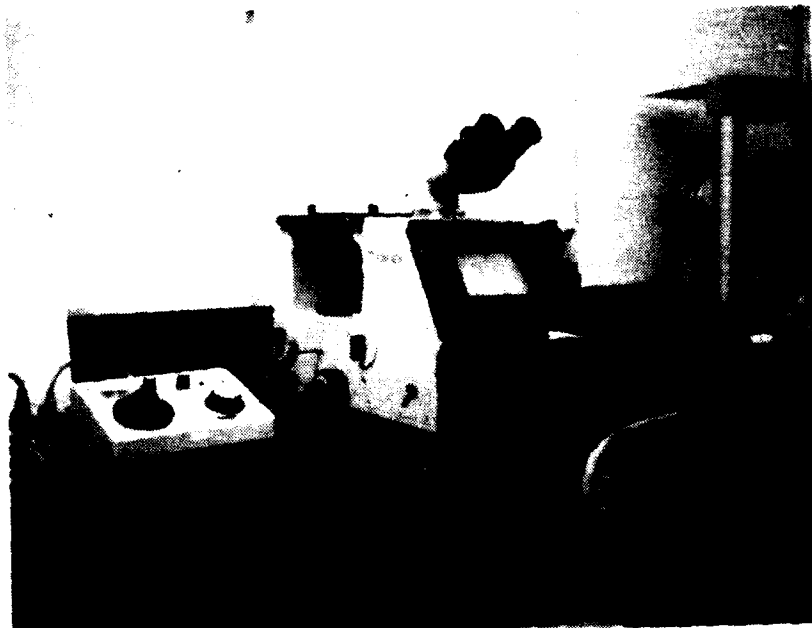


Figure 3.12 ZEISS ICM 405 INVERTED CAMERA MICROSCOPE

C. EXPERIMENTAL PROCEDURES

1. Target Description and Preparation

a. Glass

Microscope slides of soda lime glass, consisting of 73% SiO₂, 14% Na₂O, 7% CaO, 4% MgO, and 2% Al₂O₃, were cut in half to make 1"x3/2" targets. The targets were washed by hand and ultrasonic cleaned for 15 minutes in technical grade ethanol. Upon removal from the ultra sonic system, the targets were immediately rinsed with reagent grade ethanol, dried with a blow drier, and stored in a plastic case lined with silicone treated lens cloth (Sight Savers).

b. Plastic

Covers from 2"x2" polystyrene boxes (model 28130), made by the Cargille Corporation, were used for targets. Dust was blown off the covers before target irradiation with canned Freon.

2. Target Irradiation

a. Target Alignment

A HeNe laser, an alignment mirror mounted on the CO₂ laser output port, and a 10X beam expander, were utilized to align the target inside of the vacuum chamber. The CO₂ laser's initial alignment checks were conducted prior to target alignment in accordance with Appendix A.

b. Power Density

For the irradiation of the glass and plastic targets, the equipment setup was configuration 2 (Figure 3.6). The spot size was maintained at approximately 0.319 cm², and the laser output was approximately 10 joules. Before every firing, a brick was placed in the path between the beam splitter and the chamber, and the laser output was verified on the energy meter; the laser was adjusted if necessary and the energy reverified. The power density illuminating the target was determined using equation 3.1 and equipment data.

$$P_t = [EB_r L_t W_t] / [A_s B_t T] \text{ W/cm}^2 \quad (\text{eqn. 3.1})$$

P_t = target power density in W/cm² = 5.25 x 10⁶ W/cm²

E = energy meter reading in joules = 1.297 x 10⁻² J

B_r = ZnSe beam splitter reflectance = 99.38%

L_t = ZnSe lens transmittance = 98.51%

W_t = ZnSe window transmittance = 96.00%

A_s = spot size in cm² = 0.319 cm²

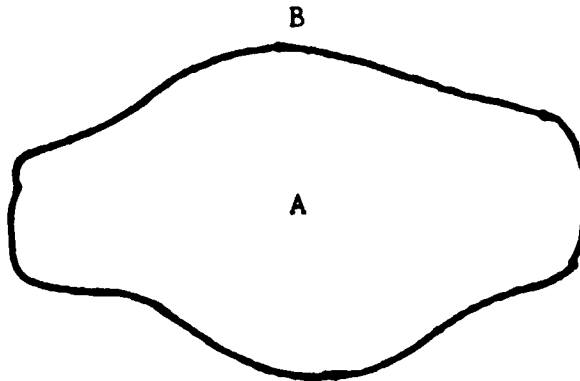
B_t = ZnSe beam splitter transmittance = 0.13%

T = Pulse Duration (FWHM) = 5.61 x 10⁻⁶ seconds

3. Target Evaluation

The Zeiss ICM 405 microscope was the primary device for target evaluation. Pictures at magnification 1000X

were used to evaluate the crater density for both the glass and plastic targets. The two locations analyzed on the glass targets are depicted in Figure 3.13.



A = Target Center

B = 2nd Point of Analysis

Figure 3.13 Glass Target's Damaged Area

The first location (position A) was located at the center of the damaged area, and the second location (position B) was located immediately outside of the heavily damaged area. The targets had orientation marks. In order to locate the same spot on each target, the microscope's reticle, in conjunction with the 50X lens, was utilized to locate the target's center (position A), and moved 2 1/2 reticle squares towards the top of the damage area (position B). This second position was outside the

exfoliation area of the glass. For the plastic targets, a point just outside the top of the damaged area was used for crater density determination. The plastic targets also had orientation marks.

Target charging prevented the use of the scanning electron microscope for target analysis. The applied, thin coats of gold or aluminum failed to make the glass conductive, and thicker coats hid the details required for analysis.

D. EXPERIMENTAL ERRORS AND LIMITATIONS

1. Experimental Error

An assessment of the experimental errors was completed using manufacturer's data, calibration reports, and the experimental results from the 100 analyzed targets.

As computed earlier, the power density at the target was 5.25×10^6 W/cm². The following statistics reflect the error of the individual components depicted in Figure 3.6:

$$U_E = \text{energy meter error} = \pm 5.0\%$$

$$U_{Br} = \text{ZnSe beam splitter reflectance error} = \pm 0.05\%$$

$$U_{Bt} = \text{ZnSe beam splitter transmittance error} = \pm 0.20\%$$

$$U_{Lt} = \text{ZnSe lens transmittance error} = \pm 0.20\%$$

$$U_{Wt} = \text{ZnSe window transmittance error} = \pm 1.5\%$$

$$U_{As} = \text{spot size error} = \pm 3.6\%$$

$$U_T = \text{pulse width error} = \pm 3.6\%$$

$$U_L = \text{fluctuation of output laser energy} = \pm 3.3\%$$

The laser output was closely monitored to improve its performance, and its precision was used as an indication of the error induced by the laser's output deviation. The standard deviation of the spot size was utilized as a measure of the spot-size error. In a worst-case situation, when all of the errors were cumulative, the power density error would be 17.5%. If equation 3.2 was used, the experimental error would be 8.0%; this equation was a better indicator of the total error since all of the errors were independent of each other.

$$U_{\text{Total}} = (U_1^2 + U_2^2 + U_3^2 + \dots + U_N^2)^{1/2} \quad (\text{eqn. 3.2})$$

The experimental error introduced by the pressure measurements was difficult to determine. The Matheson Gauge had an accuracy of $\pm 0.25\%$ of the maximum scale value equating to an error of $\pm 1.90\text{mm Hg}$. The ionization gauge and thermocouple gauge were parts of a system that was over 25 years old. The accuracy of the gauges were unobtainable, so the error was estimated at 5.0% for each gauge. Since only one pressure gauge was used per measurement, the experimental error introduced by the pressure gauges equated to approximately 5.0%.

The crater density error, introduced by the microscope's resolution capability in the counting of the craters, limited the accuracy of the crater density. Three

crater density counts per target location were conducted, and an average error of approximately 5% was attributed to the crater density calculation.

Taking into account both the pressure gauges' error, the power density error, and the crater density error, the experimental error was determined to be approximately 10%.

2. Experimental Limitations

The limitations of the experiment were mainly caused by a number of equipment shortages and shortcomings. The failure of one of the two energy meters prevented verification of the laser's output energy. The calorimeter, which had not been calibrated since 1972, verified the consistency of the laser's output, but not the accuracy. Even though three pressure gauges were utilized to determine the pressure, none of the pressure ranges overlapped; this prevented pressure accuracy verification. The thermocouple gauge (10^{-3} to 10^{-6} atmospheres) was very difficult to read precisely and sometimes acted erratically thereby limiting the accuracy of the pressure determination in that range. The CO₂ laser did not have a mode selection capability which caused a noncircular beam pattern (Figure 3.7 and 3.8). The power density at the target was not distributed in a uniform circle thereby causing a non-uniform beam pattern.

The other limitation of this experiment was the inability to examine the damaged area of the glass at a higher magnification than 1000X. Observation at higher magnification with the scanning electron microscope failed because the thin coat of gold or aluminum applied to the damaged area did not make the glass conductive enough for observation, and thicker coats hid the details. This limitation prevented close up evaluation of the individual craters. When counting the craters, the fluctuation of the crater size, combined with the magnification limitation, limited the accuracy of the crater density. It was also impossible to get an accurate crater size comparison because at a magnification of 1000X, the small craters appeared as dots. Optical magnification greater than 1000X, which required the use of oil, failed because the craters visibly disappeared when the oil was applied.

IV. EXPERIMENTAL RESULTS

A. INTRODUCTION

The experimental results are presented in this section with the primary emphasis on glass targets. Since this is the first time these measurements have been documented, several pictures have been included, and because of the complexity of the results, all macroscopic and microscopic observations are included. The glass targets' data is presented first, followed by the plastic targets' data.

B. GLASS (SODA LIME) TARGETS

1. Crater Density at the Target's Center

Ninety soda lime glass targets were irradiated with the CO₂ laser. The incident power density was approximately 5.25×10^6 W/cm² with a pulse width (FWHM) of 5.61 microseconds and a spot size of 0.319 cm². The pressure was varied from one atmosphere down to 10⁻⁸ atmosphere with the primary emphasis in the region from one atmosphere down to 10⁻⁴ atmosphere. Using the methods described in Chapter 3, the crater density at the center of the glass targets was determined on four different targets per pressure and six density calculations per target. The average and standard deviation at each pressure was computed and compiled in Table 4.1. Figure 4.1 displays these results, and Figures 4.2 through 4.11 form a crater

density progression of the target's center at magnification 1000X for pressures from one atmosphere down to 10^{-8} atmosphere. The decreased pressure initially caused a linear drop in the crater density; however at 0.2 atmosphere, the density deviated from the linear decline and reached a minimum density at 0.1 atmosphere. The crater density remained constant from 0.1 atmosphere down to 10^{-3} atmosphere after which the crater density increased. At low pressures, the crater density at the target's center was more uniformly distributed as compared to higher pressures (Figures 4.2 and 4.11). Data was not obtained between pressures of 10^{-4} and 10^{-7} atmosphere, but the crater density at 10^{-4} atmosphere and 10^{-8} atmosphere were comparable.

TABLE 4.1

CRATER DENSITY AT THE TARGET'S CENTER (GLASS)

Pressure (Atmosphere)	Average Crater Density ($\times 10^6$ Craters/cm ²)	Standard Deviation ($\times 10^6$ Craters/cm ²)
1.0	105	26.9
6.0×10^{-1}	64.3	18.0
4.0×10^{-1}	26.7	7.84
2.0×10^{-1}	12.5	5.93
1.0×10^{-1}	3.32	1.11
5.0×10^{-2}	3.33	1.41
5.0×10^{-3}	3.00	0.85
1.0×10^{-3}	9.22	3.73
5.0×10^{-4}	20.5	6.28
1.0×10^{-4}	26.9	5.36
1.3×10^{-7}	19.1	3.96
7.1×10^{-9}	22.9	6.02

(CENTER OF GLASS TARGETS)

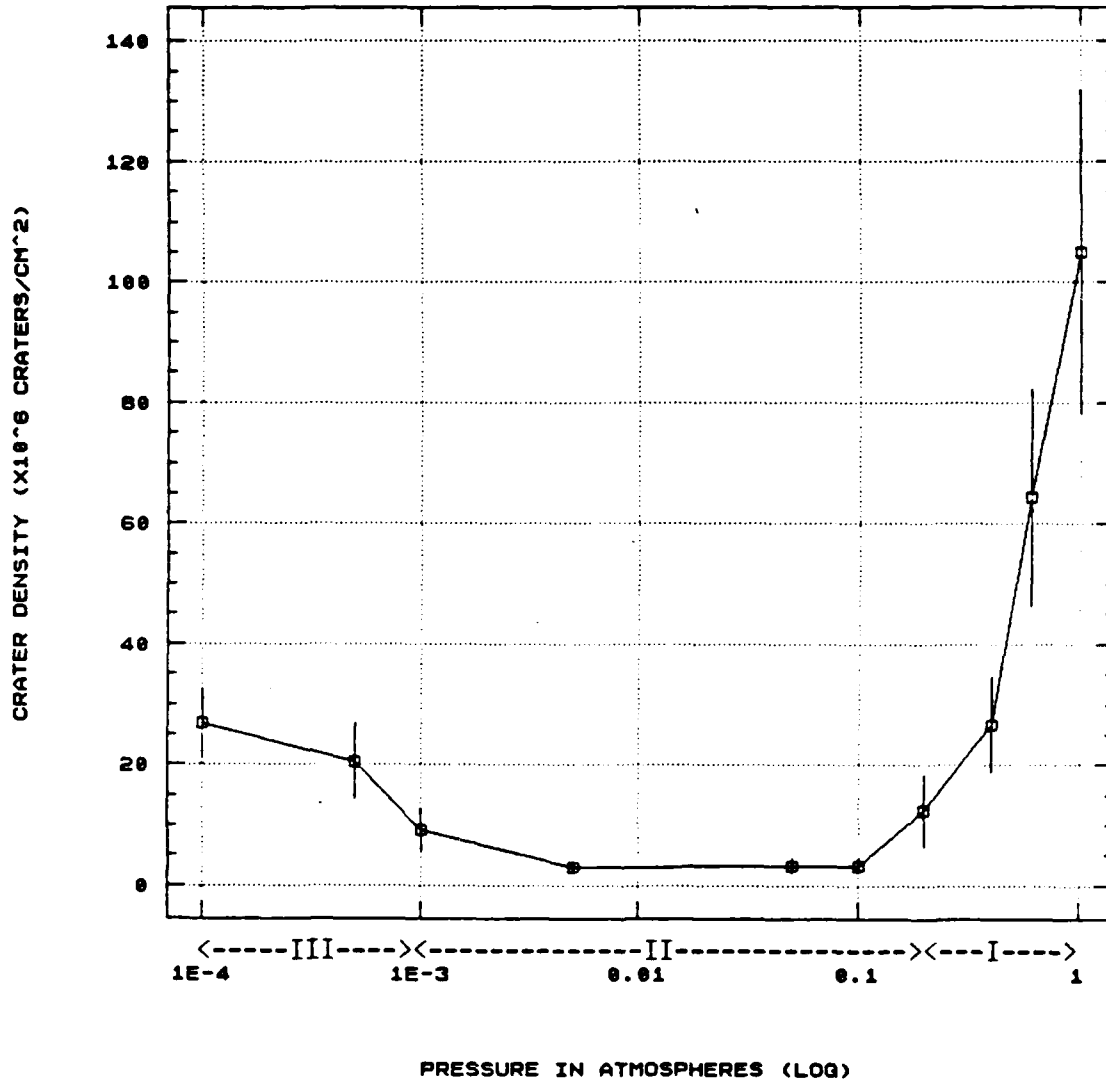


Figure 4.1 Pressure vs Crater Density (Glass) (Center)

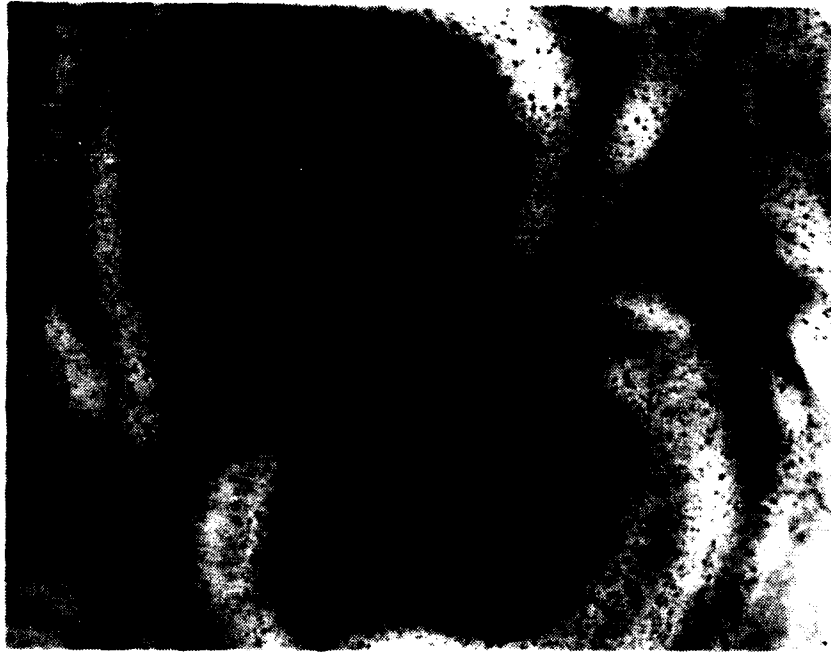


Figure 4.2 Center Crater Density (1 atm) (1000X)

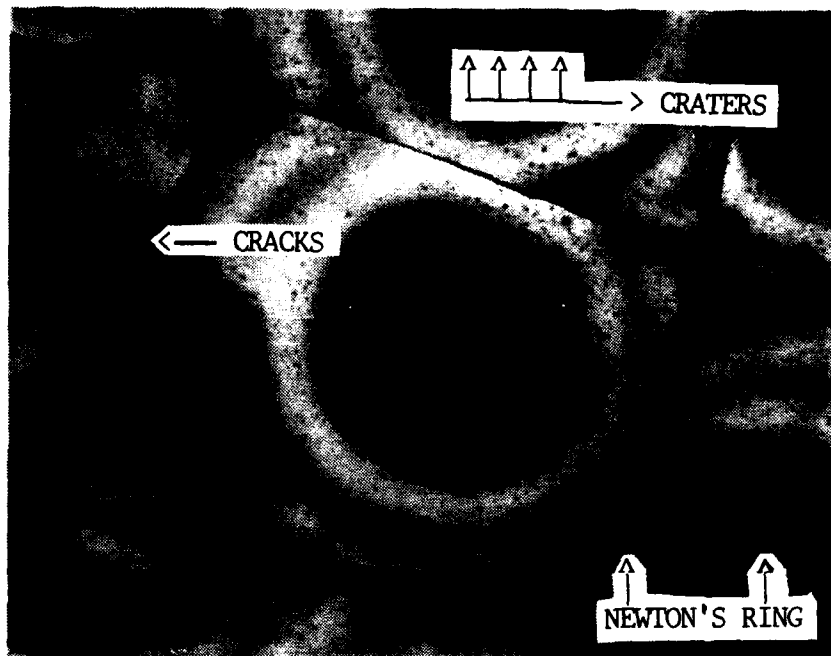


Figure 4.3 Center Crater Density (6.0×10^{-1} atm) (1000X)



Figure 4.4 Center Crater Density (2.0×10^{-1} atm) (1000X)



Figure 4.5 Center Crater Density (1.0×10^{-1} atm) (1000X)

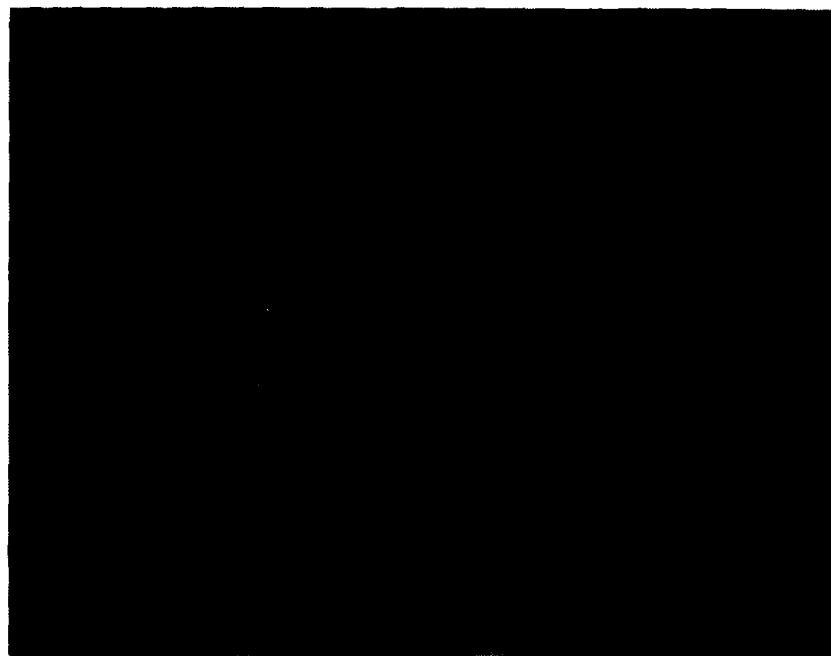


Figure 4.6 Center Crater Density (5.0×10^{-2} atm) (1000X)

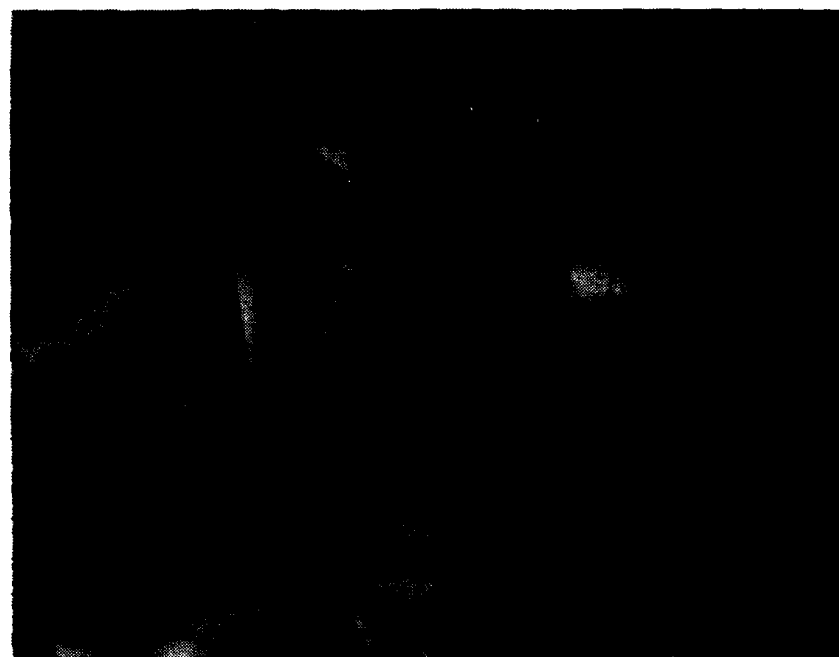


Figure 4.7 Center Crater Density (5.0×10^{-3} atm) (1000X)

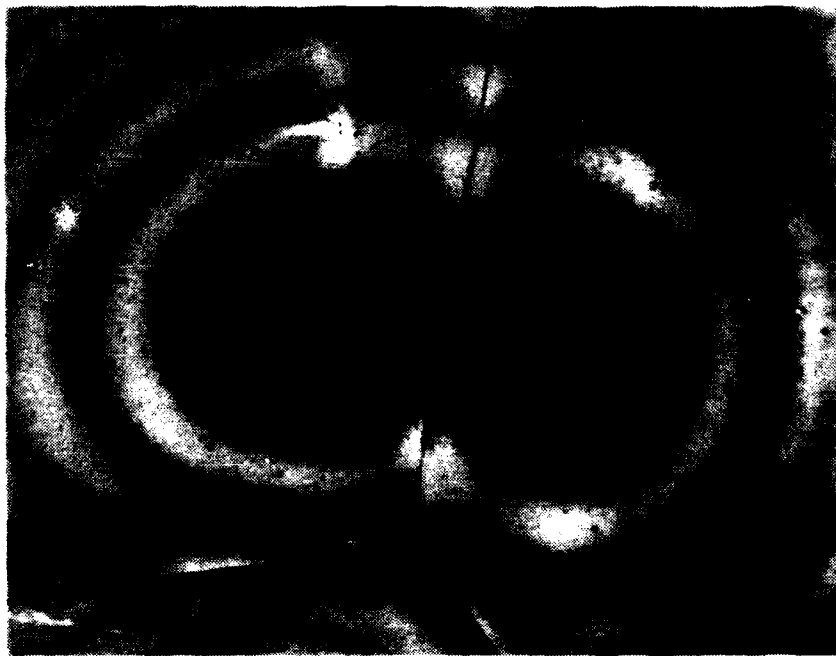


Figure 4.8 Center Crater Density (1.0×10^{-3} atm) (1000X)



Figure 4.9 Center Crater Density (5.0×10^{-4} atm) (1000X)

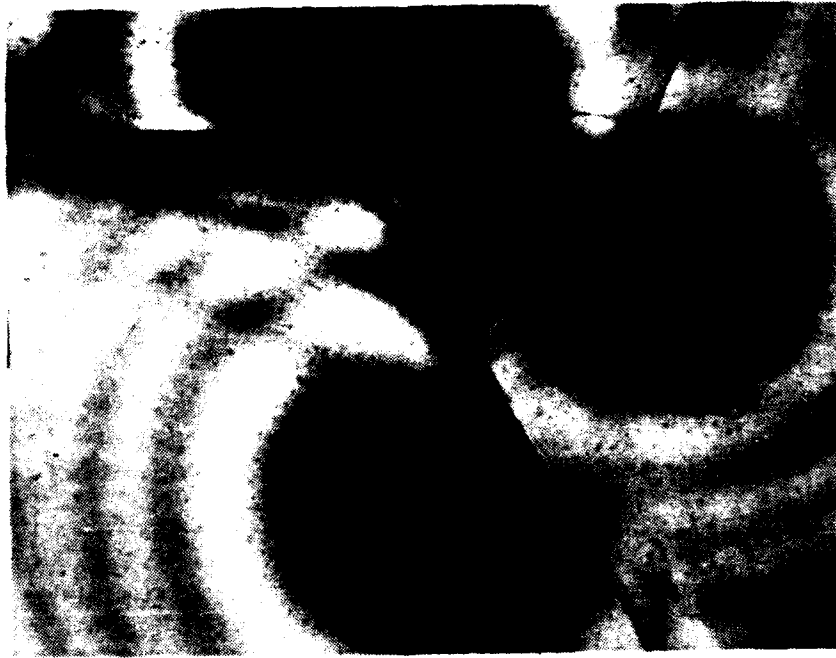


Figure 4.10 Center Crater Density (1.0×10^{-4} atm) (1000X)



Figure 4.11 Center Crater Density (7.1×10^{-9} atm) (1000X)

2. Crater Density at the Target's Perimeter

The perimeter crater density was determined outside the laser impact area and the accompanying ring pattern (point B in Figure 3.13). The density was calculated on four targets per pressure and three density calculations per target. The average and standard deviation at each pressure was computed and compiled in Table 4.2. Figure 4.12 displays these results, and Figure 4.13 through 4.20 form a perimeter crater density progression for pressures from 0.1 atmosphere down to 10^{-8} atmosphere. Perimeter craters were not observed above the pressure of 0.1 atmosphere. Between the pressures of 0.1 atmosphere and 10^{-3} atmosphere (Figures 4.13 to 4.17), the crater density remained approximately constant, and between 10^{-3} and 5.0×10^{-4} atmosphere, it rose by a factor of five (Figure 4.18). The perimeter crater density peaked somewhere between 10^{-4} and 10^{-3} atmosphere and appeared to level off at lower pressures. There were targets at pressures below 0.1 atmosphere that displayed a fern like pattern as depicted in Figure 4.21 rather than the normal uniformly distributed crater pattern. These fern like patterns appeared to be comprised of a series of very small craters. Magnifications of 1600X were required to discern the craters; however, photographic equipment at that magnification was unavailable. The fern pattern did not appear on a regular basis, but when it appeared, craters as depicted in Figures 4.13 through 4.20 were not observed.

TABLE 4.2

CRATER DENSITY AT THE TARGET'S PERIMETER (GLASS)

Pressure (Atmosphere)	Average Crater Density ($\times 10^6$ Craters/cm ²)	Standard Deviation ($\times 10^6$ Craters/cm ²)
1.0 --> 0.20	0.00	0.00
1.0×10^{-1}	3.92	0.30
5.0×10^{-2}	4.08	1.05
5.0×10^{-3}	5.06	0.78
1.0×10^{-3}	6.42	0.68
5.0×10^{-4}	31.6	4.56
1.0×10^{-4}	26.2	5.12
7.1×10^{-9}	16.0	5.95

(PERIMETER OF GLASS TARGETS)

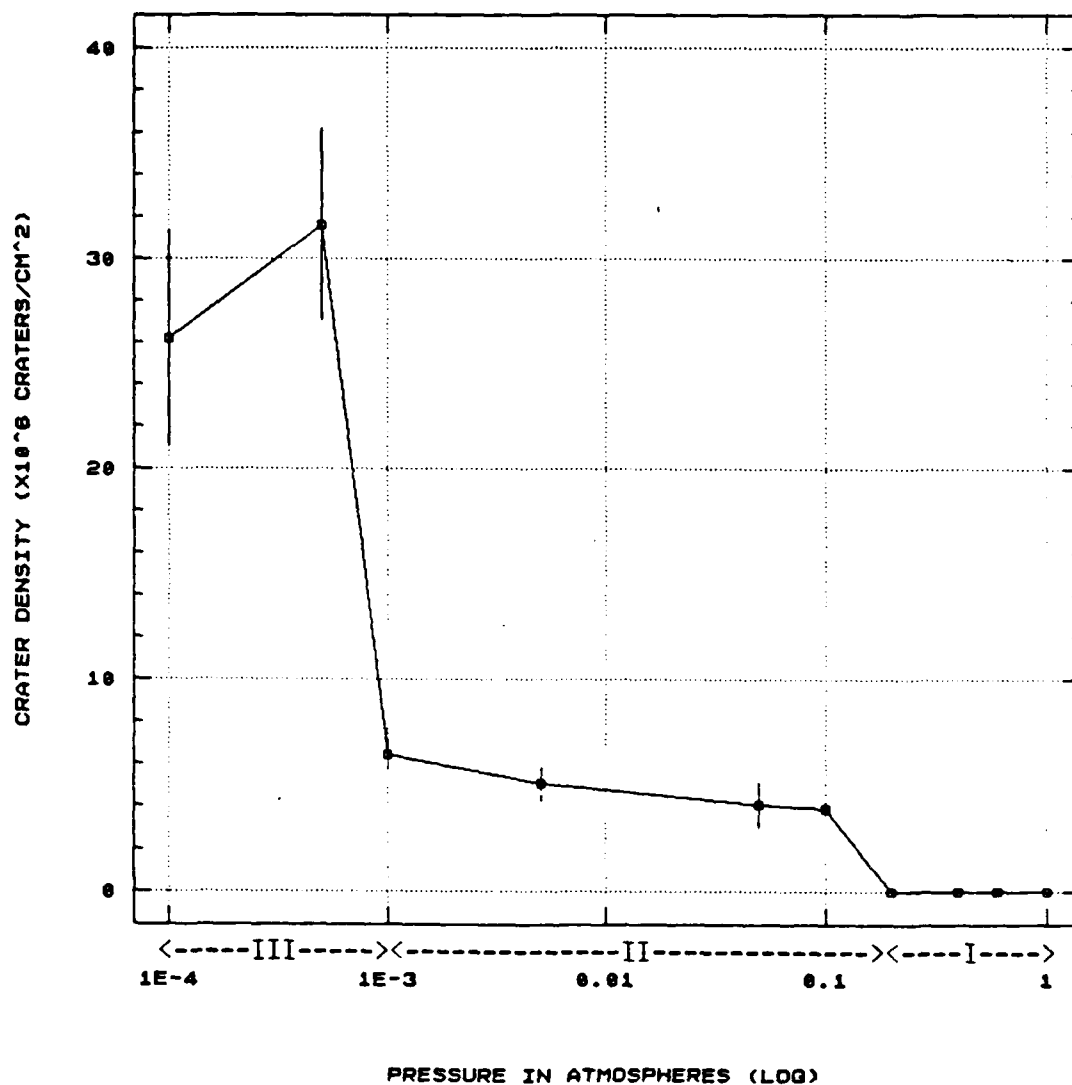


Figure 4.12 Pressure vs Crater Density (Glass) (Perimeter)



Figure 4.13 Perimeter Crater Density (1.0×10^{-1} atm) (1000X)



Figure 4.14 Perimeter Crater Density (5.0×10^{-2} atm) (1000X)



Figure 4.15 Perimeter Crater Density (5.0×10^{-3} atm) (1000X)



Figure 4.16 Perimeter Crater Density (1.0×10^{-3} atm) (1000X)

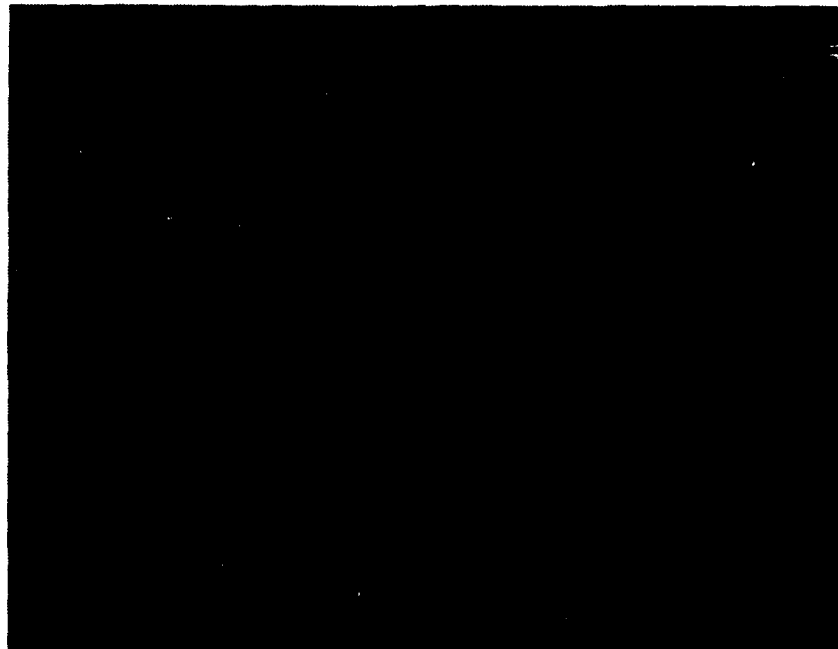


Figure 4.17 Perimeter Crater Density (1×10^{-3} atm) (1000X)



Figure 4.18 Perimeter Crater Density (5.0×10^{-4} atm) (1000X)



Figure 4.19 Perimeter Crater Density (1.0×10^{-4} atm) (1000X)



Figure 4.20 Perimeter Crater Density (7.1×10^{-9} atm) (1000X)



Figure 4.21 Fern Pattern (5.0×10^{-2} atm) (1000x)

3. Overall Target Damage

A third factor was observed to be connected to the linear deviation of the crater density at pressures below 0.2 atmosphere. As can be seen in the target damage progression in Figures 4.21 through 4.35, the ring pattern at the target perimeter shifts radially outward between 0.2 atmosphere (Figure 4.26) and at 10^{-3} atmosphere (Figure 4.32). This pressure range corresponds to the plateaus in the crater density graphs (Figure 4.1 and 4.12). It was also noted that the craters outside the laser impact area appeared when the target's ring started its outward shift. Once the ring was totally formed into two circular rings (Figure 4.33), the crater density increased at both the

target's center and perimeter. More in depth pictures were taken of each ring to gain insight into its crater density connection. Figures 4.36 through 4.47 are pictures of the ring progression at 100X, and Figures 4.48 through 4.56 are pictures of the ring progression at 1000X. Between one atmosphere and 0.2 atmosphere, the target's single ring remained a fixed displacement immediately outside of the cracked glass area (Figures 4.22 and 4.26). It appeared to be formed by an enhanced damage pattern and melting of the glass (Figure 4.36 to 4.38 and 4.48 to 4.50). From 0.1 atmosphere to 0.001 atmosphere, the ring shifted outward in a wave type pattern (Figure 4.27 to 4.32 and 4.39 and 4.44), and as many as three different rings (Figure 4.29) were observed shifted away from the laser beam impact area. In Figures 4.39 to 4.47 and 4.51 to 4.56, these rings seemed to focus into a circular pattern, and the damage intensity decreased as the pressure decreased. These focussed rings consisted of an inner ring, which was approximately 3.6 millimeters from the center of the target, and the outer ring, which was approximately 4.2 millimeters from the center of the target. These rings remained at a fixed distance from the target's center for pressures of 0.001 atmosphere and below. It was noted that as the pressure decreased, the flash produced in the vacuum chamber reduced in intensity, and the light emitted changed from a bright, white florescent-type emission to a dull,

incandescent-type emission. It was also noted that the glass plates' rear surface was not damaged at any pressure.

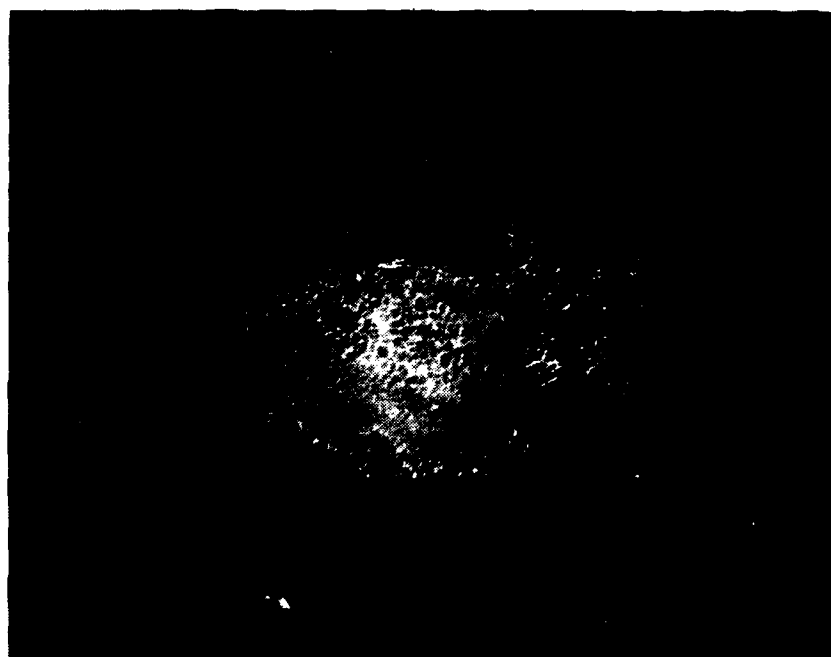


Figure 4.22 Target Damage at 1 Atm (10X)

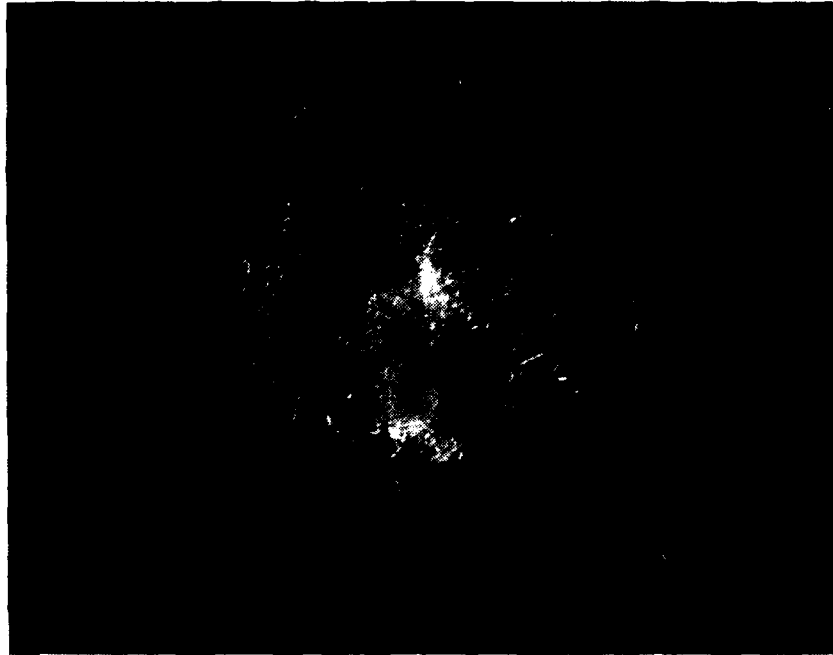


Figure 4.23 Target Damage at 8.0×10^{-1} Atm (10X)

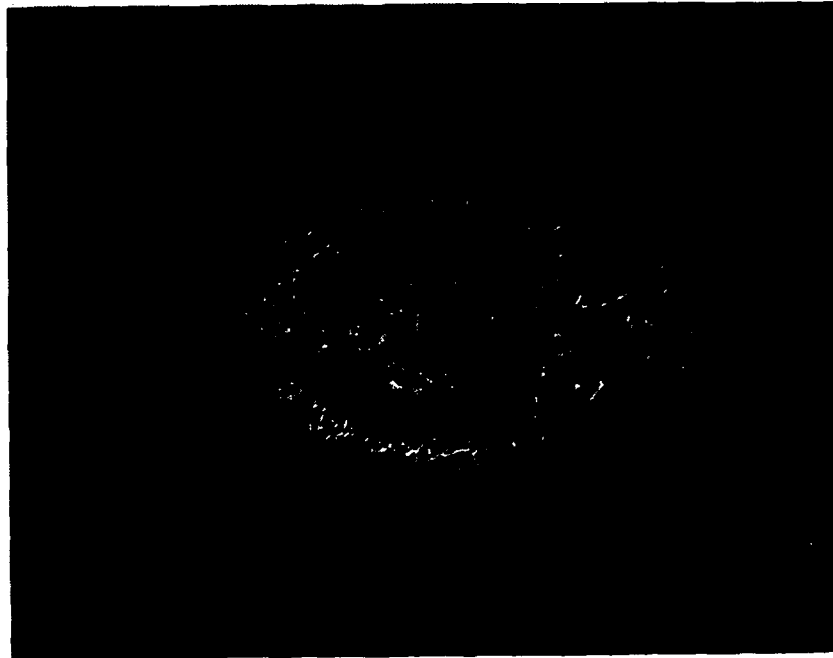


Figure 4.24 Target Damage at 6.0×10^{-1} Atm (10X)



Figure 4.25 Target Damage at 4.0×10^{-1} Atm (10X)

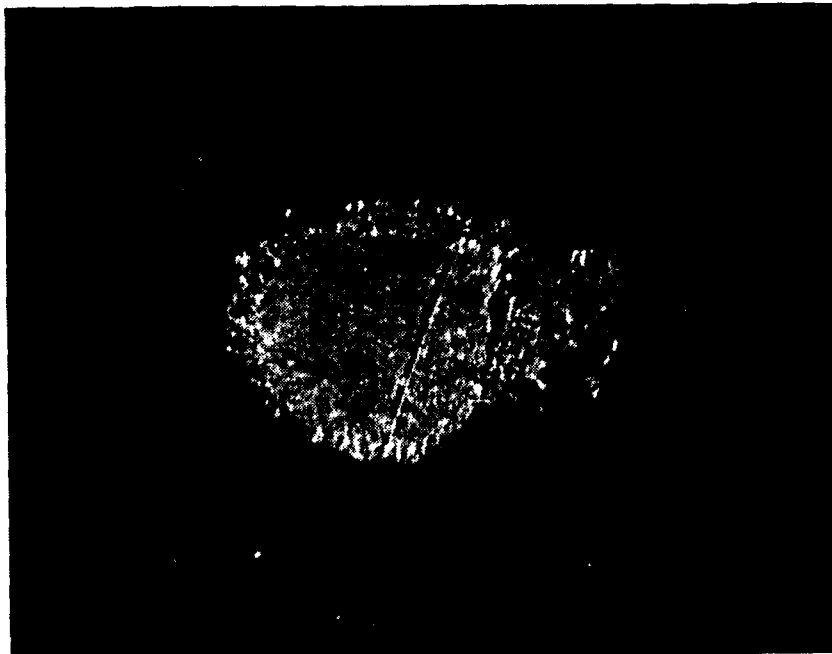


Figure 4.26 Target Damage at 2.0×10^{-1} Atm (10X)

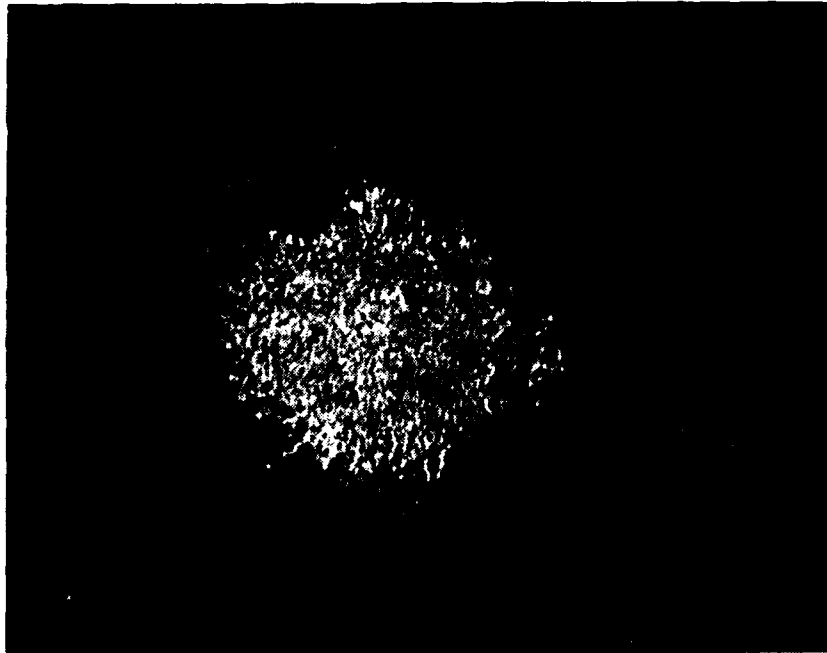


Figure 4.27 Target Damage at 1.0×10^{-1} Atm (10X)



Figure 4.28 Target Damage at 5.0×10^{-2} Atm (10X)

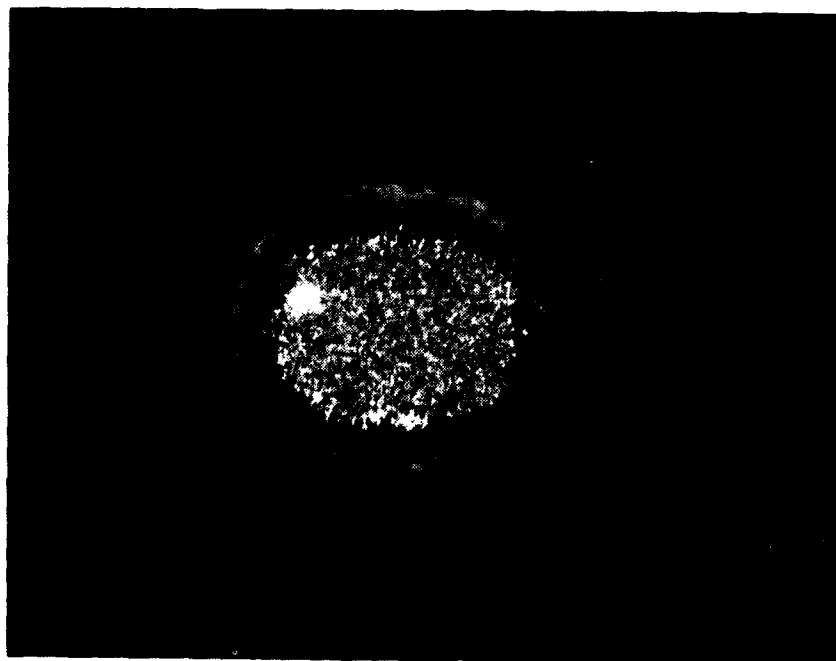


Figure 4.29 Target Damage at 2.5×10^{-2} Atm (10X)

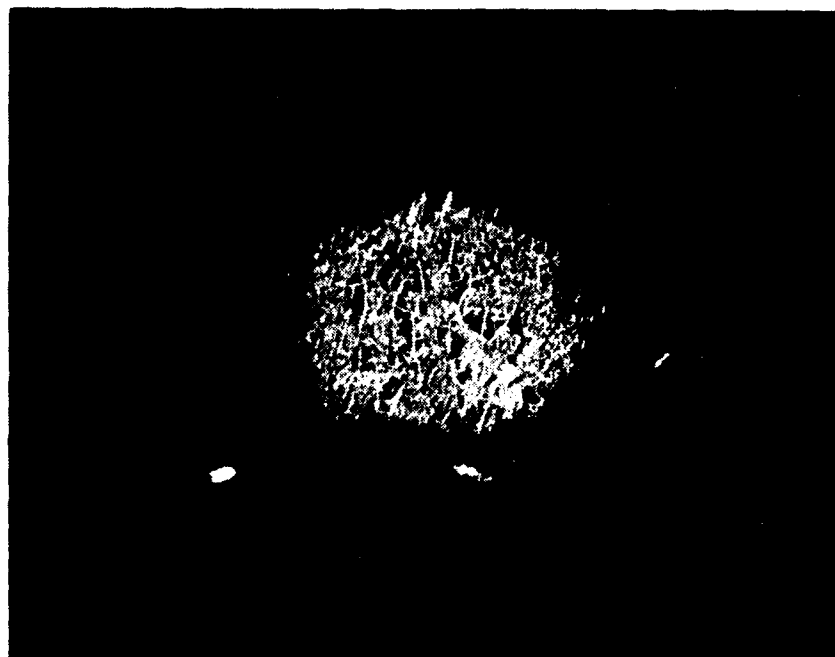


Figure 4.30 Target Damage at 1.25×10^{-2} Atm (10X)

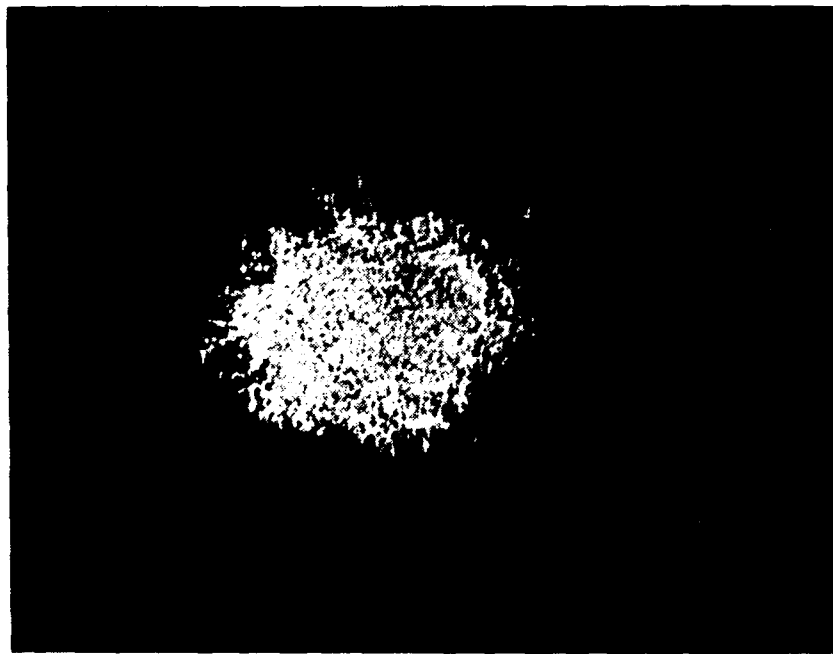


Figure 4.31 Target Damage at 5.0×10^{-3} Atm (10X)

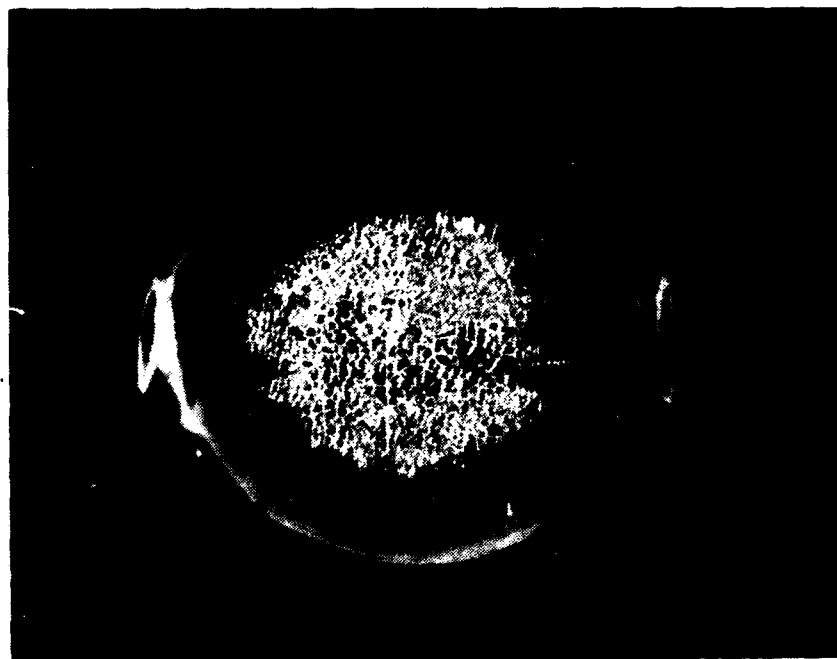


Figure 4.32 Target Damage at 1.0×10^{-3} Atm (10X)

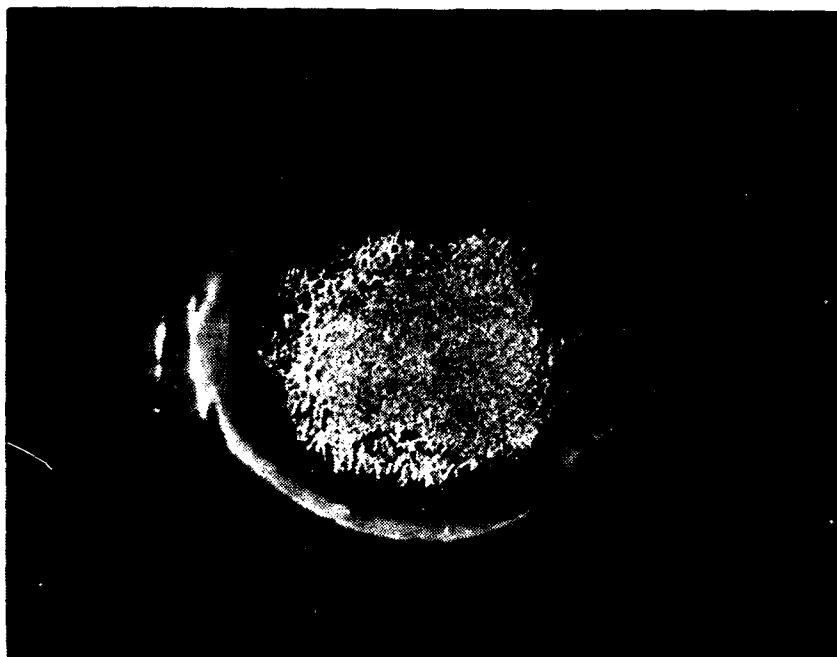


Figure 4.33 Target Damage at 5.0×10^{-4} Atm (10X)



Figure 4.34 Target Damage at 1.0×10^{-4} Atm (10X)



Figure 4.35 Target Damage at 1.3×10^{-7} Atm (10X)



Figure 4.36 Ring Damage at 1.0 Atm (100X)



Figure 4.37 Ring Damage at 6.0×10^{-1} Atm (100X)

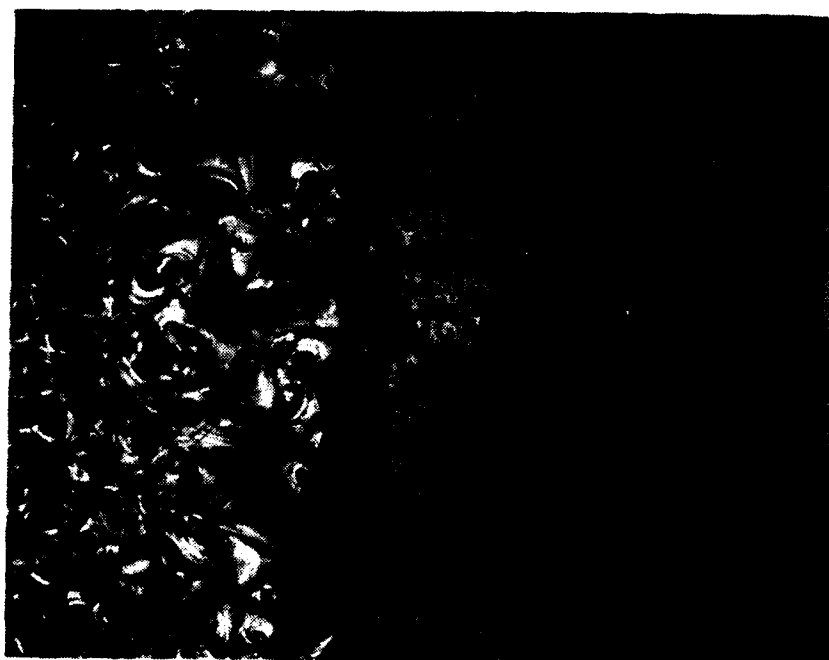


Figure 4.38 Ring Damage at 2.0×10^{-1} Atm (100X)



Figure 4.39 Ring Damage at 1.0×10^{-1} Atm (100X)

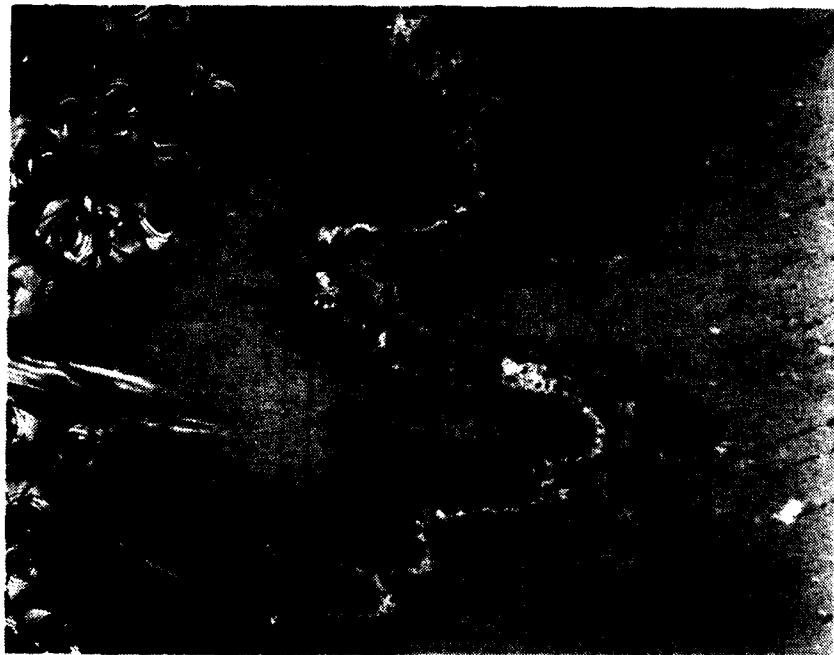


Figure 4.40 Ring Damage at 5.0×10^{-2} Atm (100X)

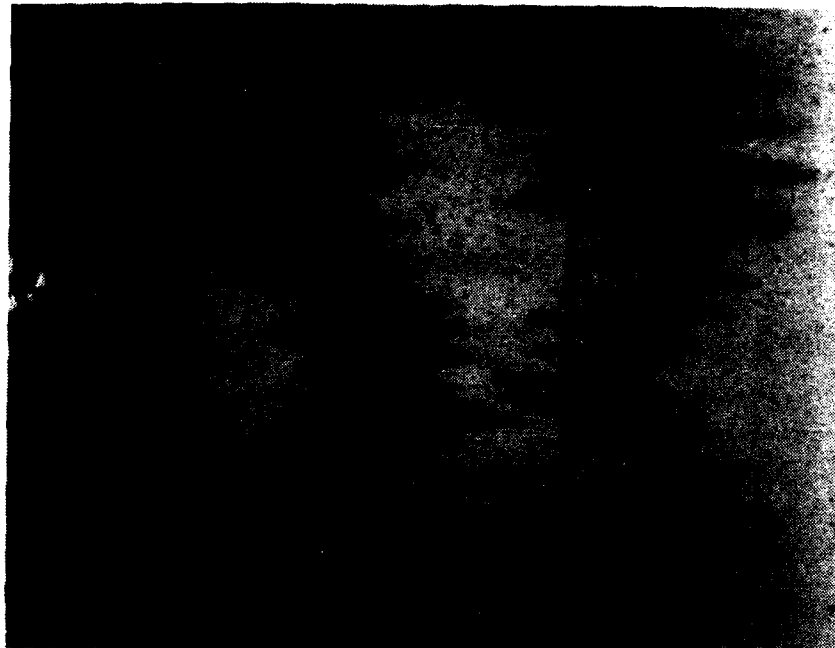


Figure 4.41 Ring Damage at 1.25×10^{-2} Atm (100X)



Figure 4.42 Ring Damage at 2.5×10^{-2} Atm (100X)

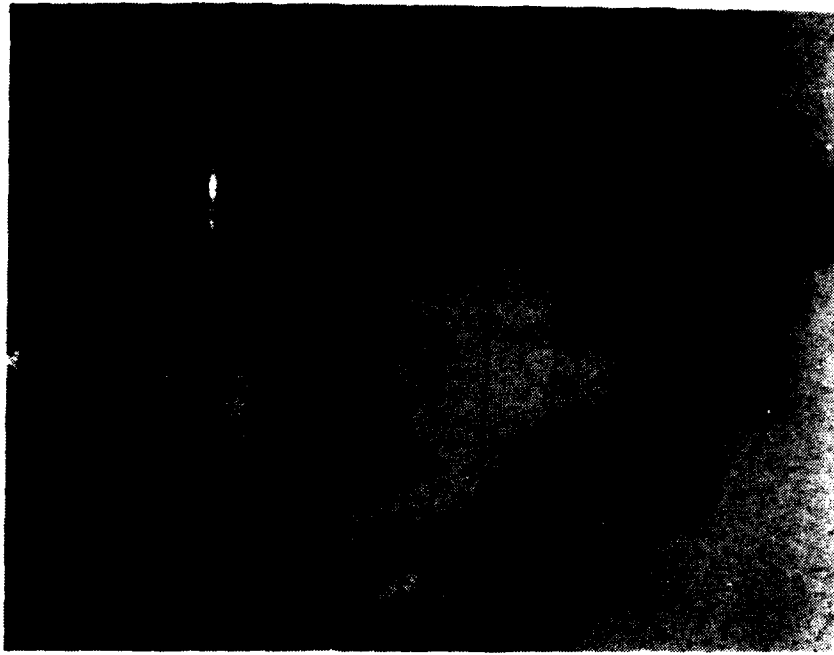


Figure 4.43 Ring Damage at 5.0×10^{-3} Atm (100X)

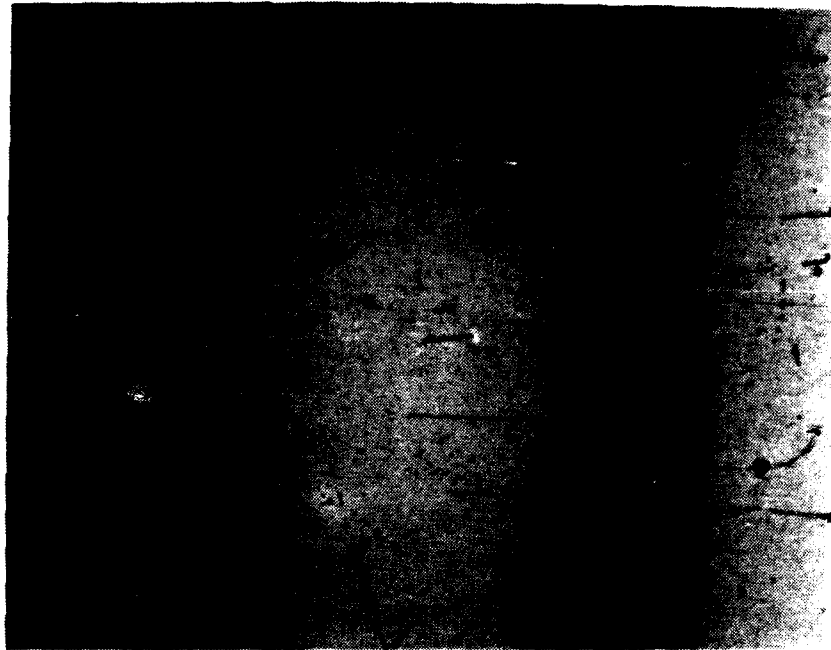


Figure 4.44 Ring Damage at 1.0×10^{-3} Atm (100X)

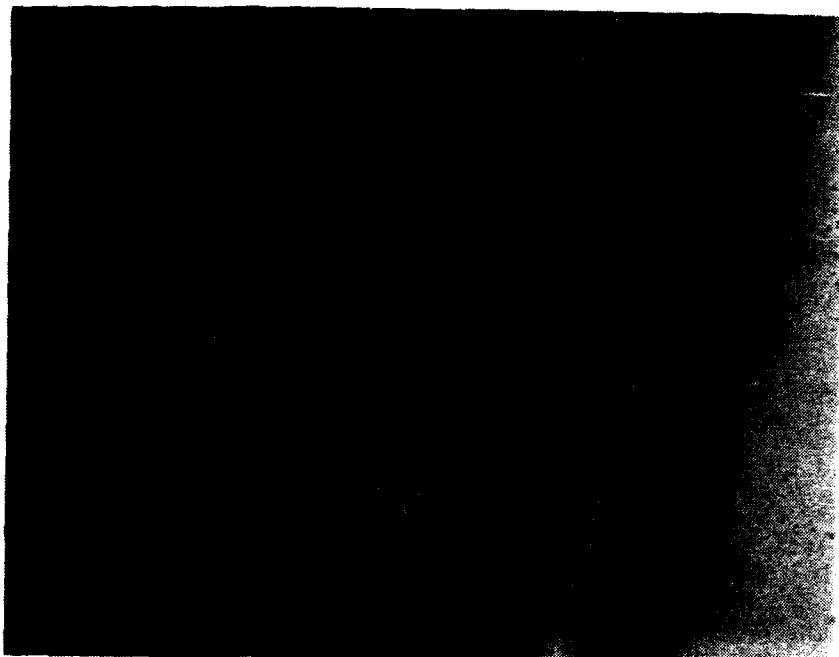


Figure 4.45 Ring Damage at 5.0×10^{-4} Atm (100X)

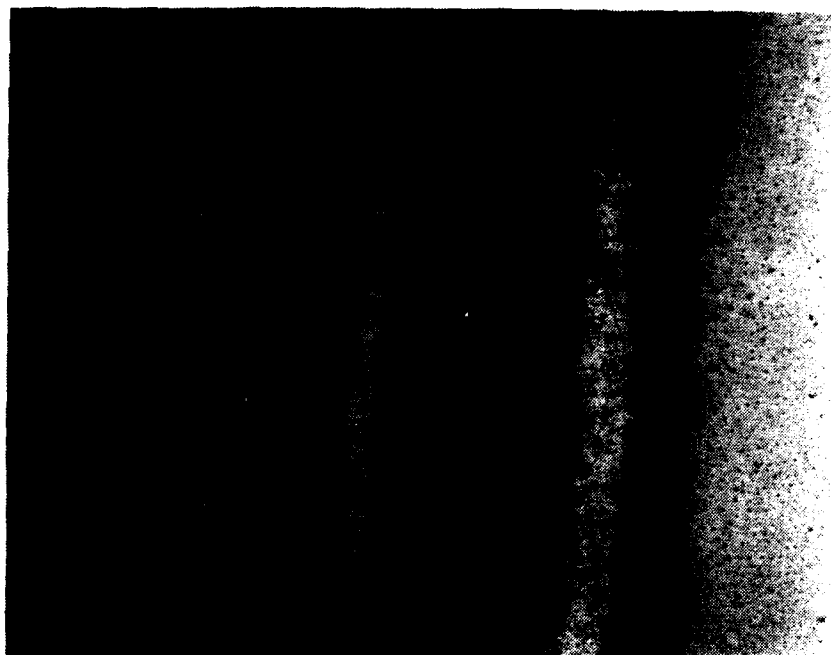


Figure 4.46 Ring Damage at 1.0×10^{-4} Atm (100X)

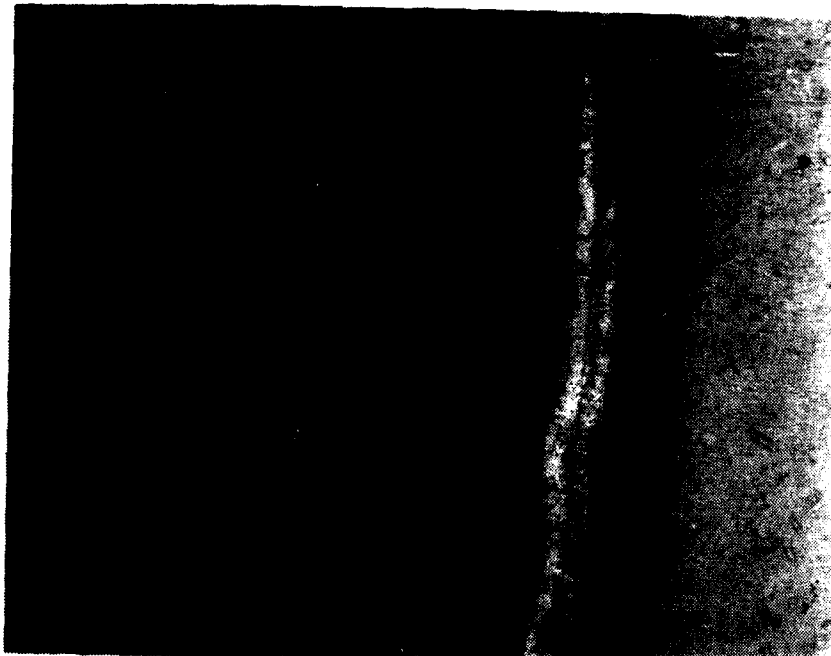


Figure 4.47 Ring Damage at 1.3×10^{-7} Atm (100X)



Figure 4.48 Ring Damage at 1.0 Atm (1000X)



Figure 4.49 Ring Damage at 2.0×10^{-1} Atm (outside) (1000X)



Figure 4.50 Ring Damage at 2.0×10^{-1} Atm (inside) (1000X)



Figure 4.51 Ring Damage at 1.0×10^{-1} Atm (1000X)

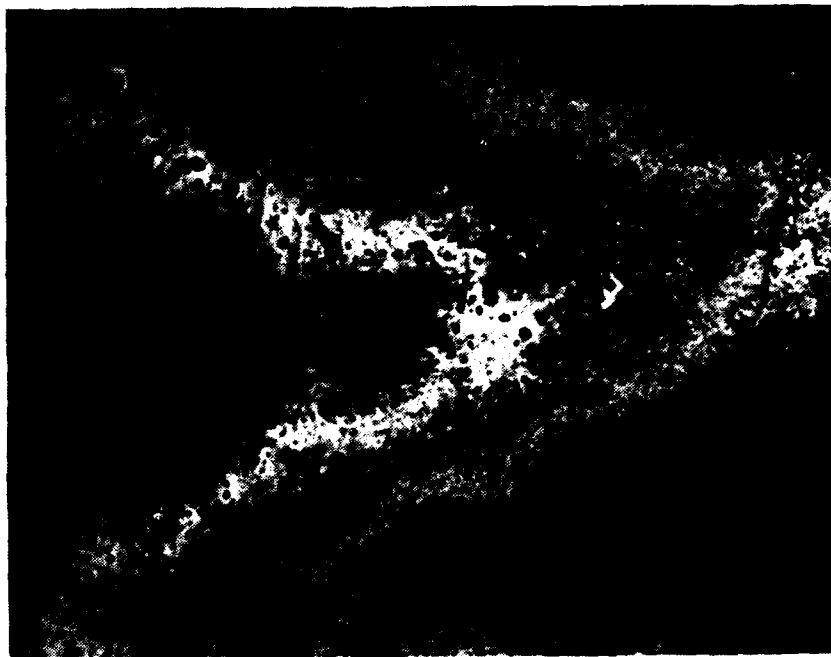


Figure 4.52 Ring Damage at 5.0×10^{-2} Atm (1000X)

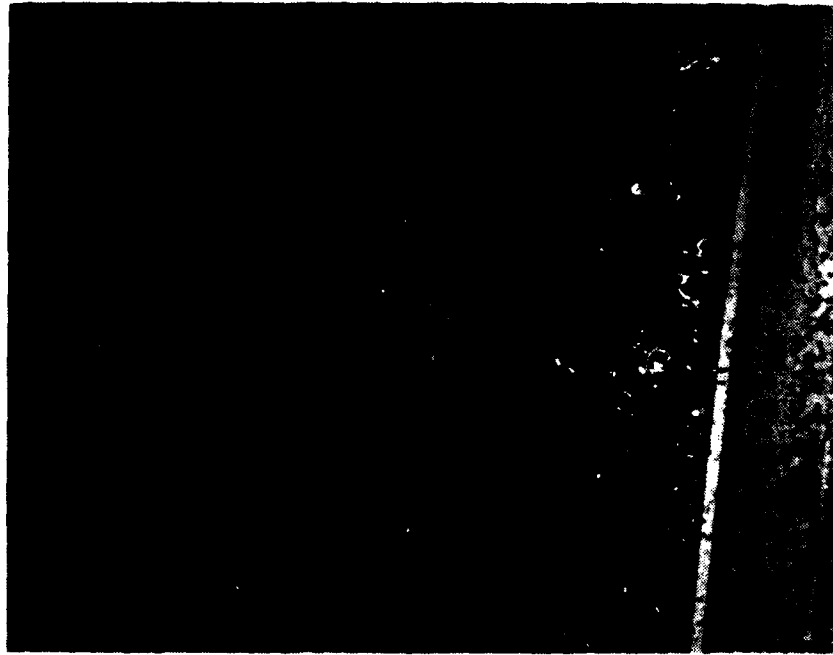


Figure 4.53 Ring Damage at 1.25×10^{-2} Atm (Inner Ring) (1000X)



Figure 4.54 Ring Damage at 1.25×10^{-2} Atm (Outer Ring) (1000X)



Figure 4.55 Ring Damage at 1.0×10^{-3} Atm (1000X)



Figure 4.56 Ring Damage at 1.0×10^{-4} Atm (1000X)

4. Discussion and Summary of Glass Target's Results

In order to develop a full picture of the crater density's pressure dependence, the crater density at the target's perimeter and at the center were plotted against pressure (Figure 4.57). The pressure dependence can be separated into three ranges as depicted in the figure. In range one (1 - 0.1 atm), there was a linearly decreasing pressure dependence of the crater density at the target's center, craters were not present at the perimeter of the heavily damaged area, there was a bright white florescent-type flash upon target illumination, and the ring pattern remained fixed around the edge of the exfoliation area. In range two (0.1 - 0.001 atm), there was a constant minimal crater density at the target's center indicating that there was a reduction in irradiance at target illumination, there was a constant crater density at the perimeter, and there was outward shift of the surrounding ring as if caused by an acoustical-type wave. In range three (below 0.001 atm), there was an initial increase, by a factor of five, of the crater density at the target's center which dropped off slightly to a constant value at lower pressures. Likewise, the perimeter crater density initially rose to a peak and appeared to level off. There was a dull incandescent-type flash upon target illumination, and the double ring, which formed in region two, remained a fixed distance away from the target's center.

(CENTER AND PERIMETER OF GLASS TARGETS)

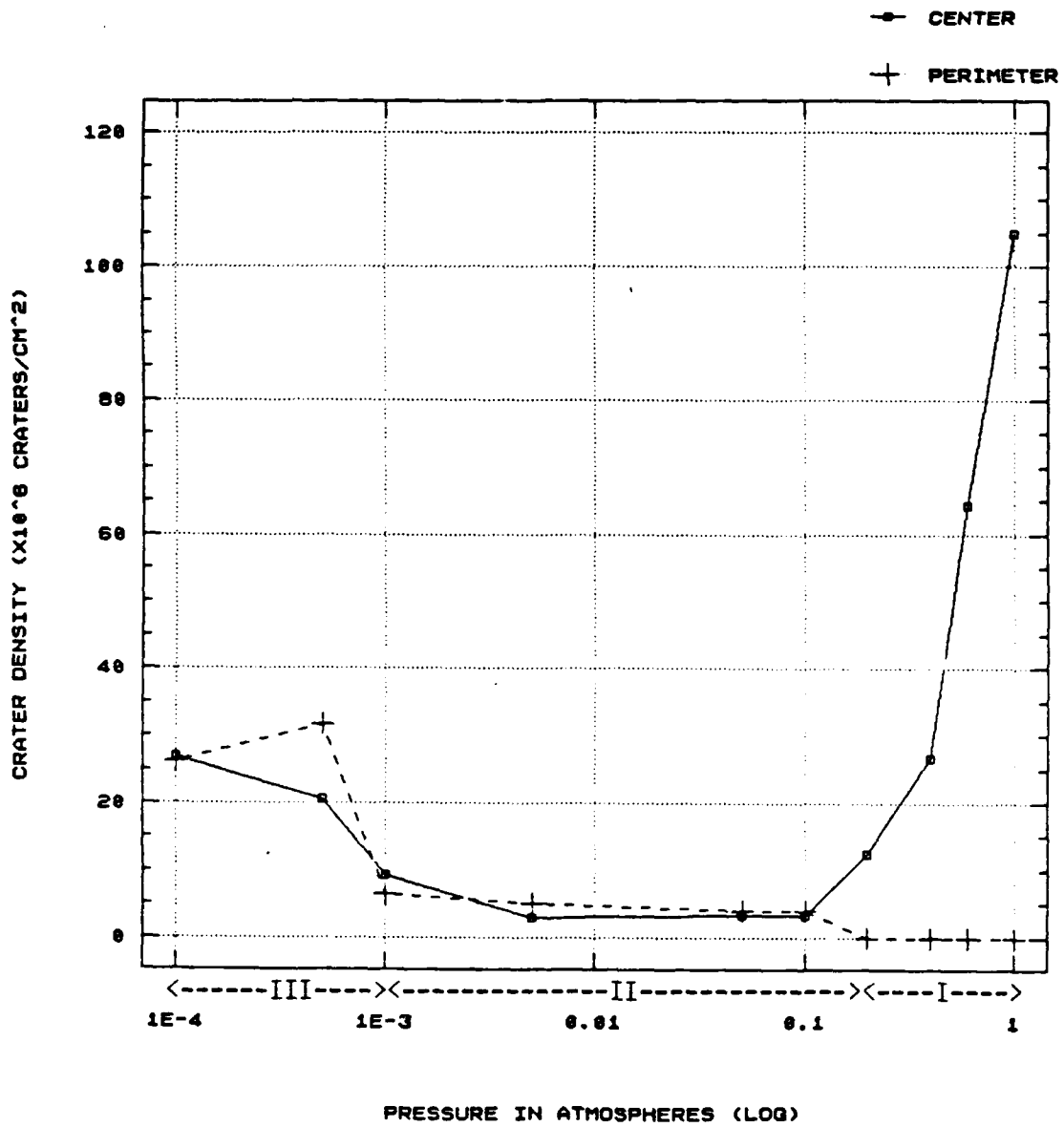


Figure 4.57 Pressure vs Crater Density (Glass)

A summary of the three pressure ranges' characteristics is listed below:

1. Region I (1 - 0.1 atm)
 - a. Linear drop in center crater density.
 - b. No perimeter craters.
 - c. Bright white florescent-type flash upon illumination.
 - d. Surrounding ring was located immediately around the edge of the cracked glass area.
2. Region II (0.1 - 0.001 atm)
 - a. Constant minimal center crater density.
 - b. Constant perimeter crater density.
 - c. Reduced intensity of flash.
 - d. Surrounding ring shifted outward as if caused by an acoustical-type wave.
3. Region III (below 0.001 atm)
 - a. Increased uniformly distributed, center crater density.
 - b. Increased perimeter crater density that peaked and then dropped off slightly to a constant value.
 - c. Dull incandescent-type flash.
 - d. Surrounding ring remained a fixed distance from the target's center.

In all three pressure ranges, the glass targets had approximately the same size area of cracked glass. It was

noted that all targets contained a central, circular area where the scales were approximately the same size. Immediately outside of this area, the scales were larger and the cracks tended to extend radially. At the perimeter area, some very long straight cracks were observed on an irregular basis (Figure 4.50). It was also noted that the distance from the target's center to the partial ring, evident in the burn pattern of Figure 3.7, corresponded to the ring pattern at pressures below 10^{-3} atmosphere. Other correlations between the pressure and the crater density failed. Two examples of explored correlations were the crater density size and the maximum distance from the target center that craters were observed. At the lower pressures, these two parameters seemed to increase; however, the observed results could not be supported by numerical analysis.

C. PLASTIC (POLYSTYRENE) TARGETS

1. Crater Density at the Target's Perimeter

Sixteen plastic (polystyrene) targets were irradiated with the CO_2 laser. The incident power density was approximately 5.25×10^6 W/cm^2 with a pulse width (FWHM) of 5.61 microseconds and a spot size of 0.319 cm^2 . The pressure was varied from one atmosphere down to 10^{-8} atmosphere with the primary emphasis in the region from one atmosphere down to 10^{-4} atmosphere. Using the methods described in Chapter 3, the crater density at the perimeter

of the plastic targets was determined on two different targets per pressure and four density calculations per target. The average and standard deviation at each pressure was computed and compiled in Table 4.3. Figure 4.58 displays these results, and Figures 4.59 through 4.62 form a crater density progression of the target's perimeter at magnification 1000X for pressures from 0.05 atmosphere down to 10^{-8} atmosphere. Between one atmosphere and 0.15 atmosphere, craters were not observed outside of the laser beam impact area; however at 0.05 atmosphere, craters first appeared and their density continued to increase until 5.0×10^{-4} atmosphere. Even though data was not obtained between 10^{-4} atmosphere and 10^{-8} atmosphere, it appeared that the crater density peaked at approximately 5.0×10^{-4} atmosphere and remained constant for lower pressures. The laser beam impact area experienced massive melting which destroyed any evidence of unipolar arcing in that area.

TABLE 4.3

CRATER DENSITY AT THE TARGET'S PERIMETER (PLASTIC)

Pressure (Atmosphere)	Average Crater Density ($\times 10^5$ Craters/cm 2)	Standard Deviation ($\times 10^5$ Craters/cm 2)
1.0 --> 0.15	0.00	0.00
5.0×10^{-2}	0.560	0.931
5.0×10^{-3}	6.11	2.30
5.0×10^{-4}	24.9	4.70
1.3×10^{-7}	26.0	5.93
7.1×10^{-9}	26.4	6.80

(PERIMETER OF DAMAGED AREA)

(PLASTIC TARGETS)

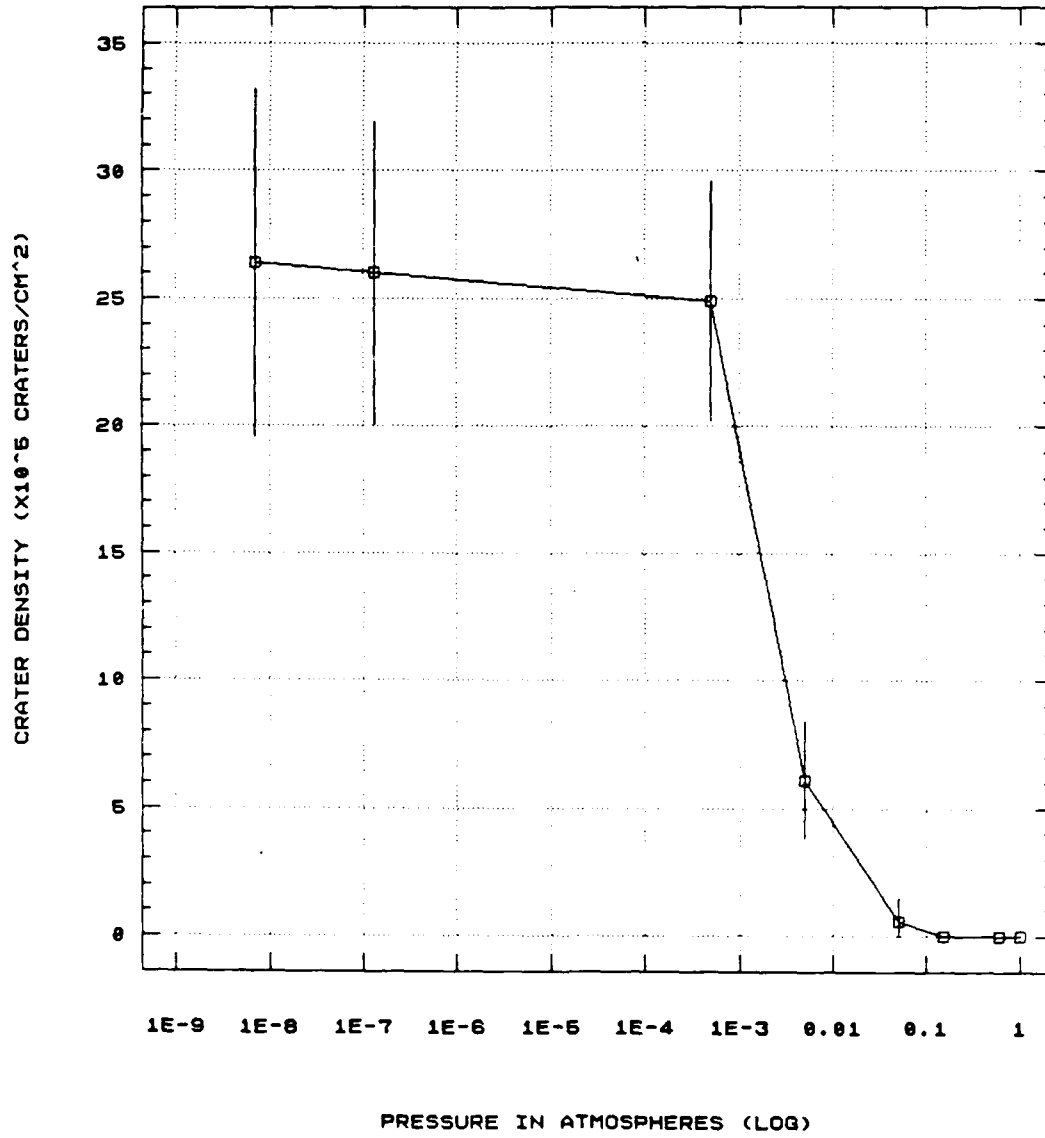


Figure 4.58 Pressure vs Crater Density (Plastic)



Figure 4.59 Perimeter Crater Density (5.0×10^{-2} atm) (1000X)

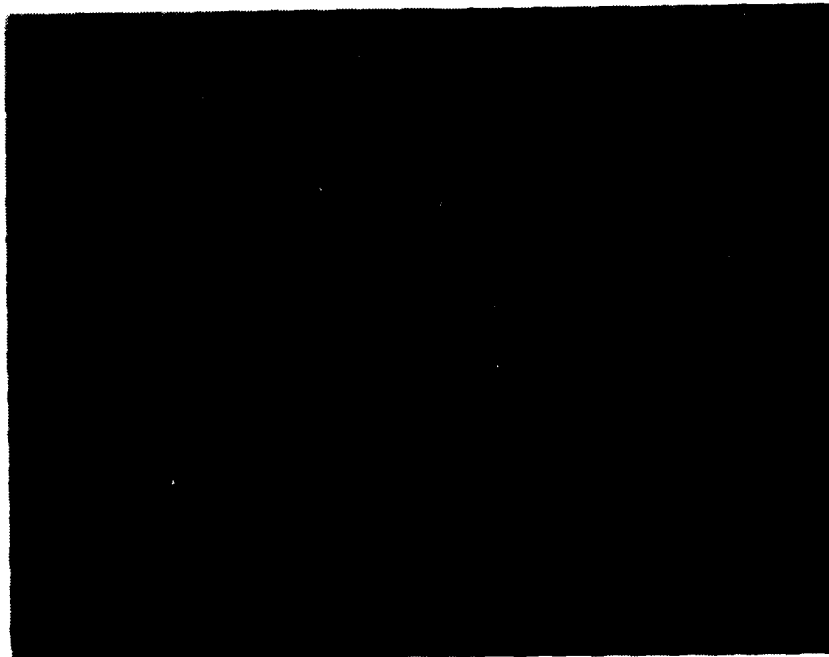


Figure 4.60 Perimeter Crater Density (5.0×10^{-3} atm) (1000X)

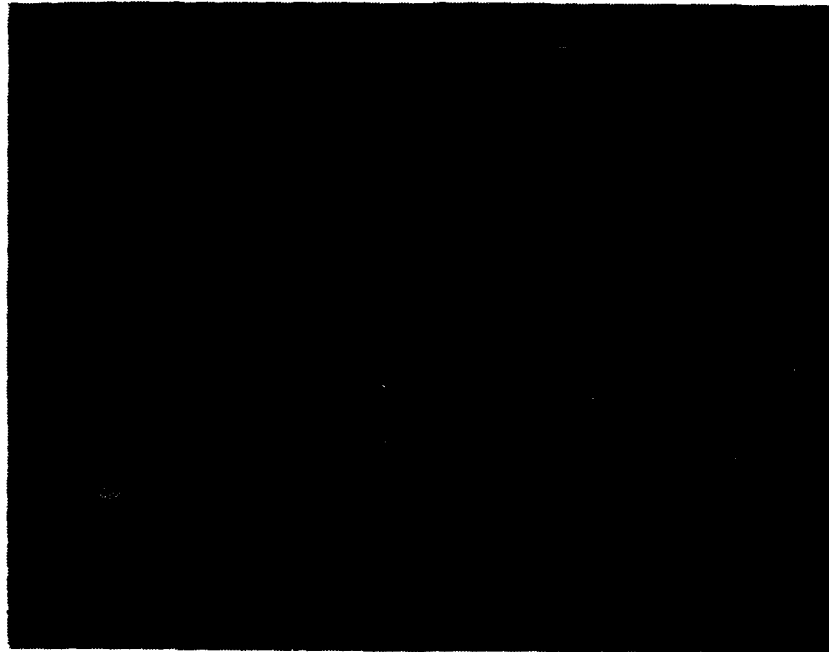


Figure 4.61 Perimeter Crater Density (5.0×10^{-4} atm) (1000X)

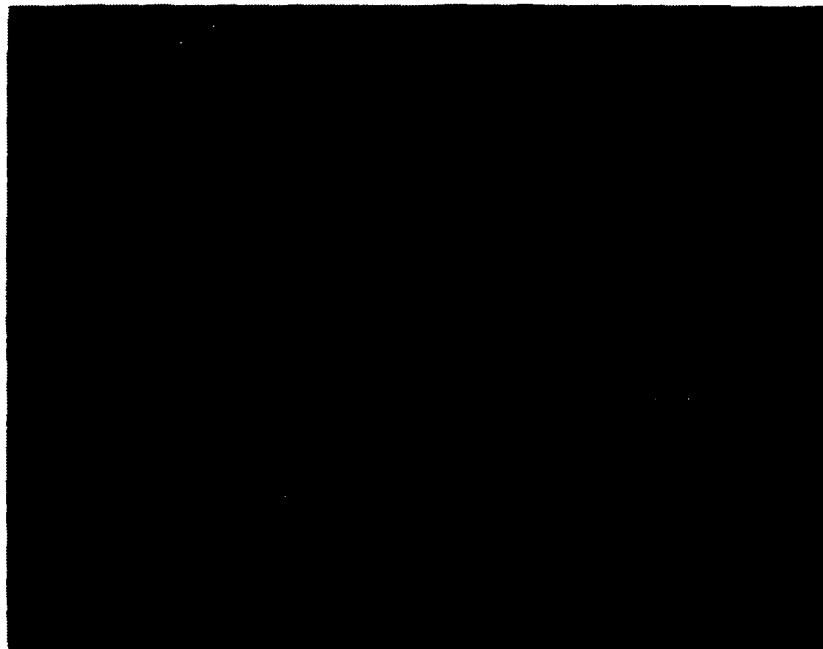


Figure 4.62 Perimeter Crater Density (7.1×10^{-9} atm) (1000X)

2. Overall Target Damage

The following observations were noted about the overall target damage. The plastic target's damaged area remained a constant size at all pressures, and unlike the glass targets, a ring did not form around the laser beam impact area at any pressure (Figures 4.63 and 4.64). This impact area experienced massive melting. As the pressure decreased, the tendency for melted plastic to splatter outside of the laser impact area increased (Figure 4.65) and the observed flash changed from a bright florescent-type to a dull incandescent-type flash.

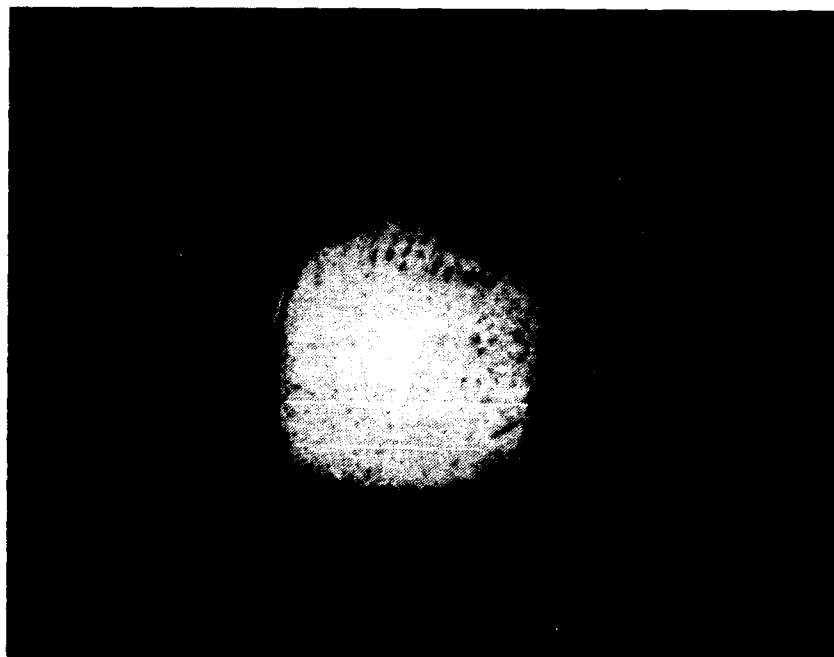


Figure 4.63 Target Damage at 1.0 Atm (10X)

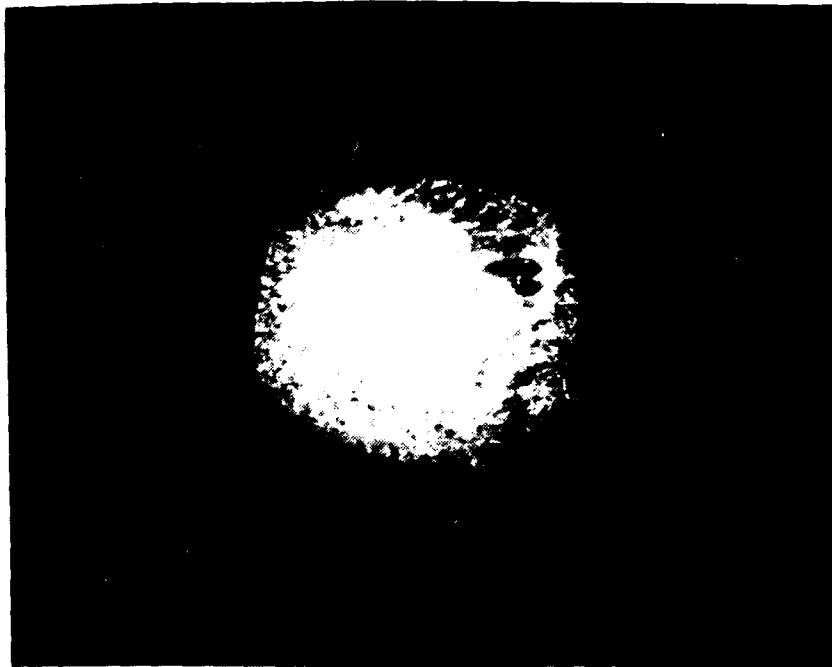


Figure 4.64 Target Damage at 5.0×10^{-4} Atm (10X)



Figure 4.65 Splattering of Material (5.0×10^{-4} Atm) (50X)

3. Discussion and Summary of Plastic Target's Results

In order to develop a full picture of the crater density's pressure dependence, Figure 4.58 was separated into three pressure ranges. In range one (1 - 0.15 atm), craters were not observed, there was a bright florescent-type flash upon target irradiation, and splattering of material outside of the impact area was not prevalent. In range two (0.15 - 0.0005 atm), the perimeter craters appeared and their intensity increased. The intensity of the flash decreased, and the splattering of melted material became more prevalent. In range three (below 0.0005 atm), it appeared that the perimeter crater density remained constant, dull incandescent-type flashes were observed at target illumination, and splattering outside of the impact area was present on all samples except one. A summary of these region's characteristics is listed below:

1. Region I (1 - 0.15 atm)
 - a. Perimeter craters were not observed.
 - b. Bright florescent-type flash.
 - c. Splattering outside of impact area was rare.
2. Region II (0.15 - 0.0005 atm)
 - a. Perimeter craters appeared and their density increased.
 - b. Lower intensity flash.
 - c. Splattering outside of impact area occurred.

3. Region III (below 0.0005 atm)

- a. Perimeter crater density appeared to remain constant.
- b. Dull incandescent-type flash.
- c. Splattering outside of impact occurred.

In all three pressure ranges, the plastic target's damaged area was approximately the same size, and cracking was not observed at any pressure. Other correlations between the pressure and the crater density failed. Two examples of explored correlations were the crater density size and the maximum distance from the target center that craters were observed. At the lower pressures, these two parameters seemed to increase; however, the observed results could not be supported by numerical analysis.

V. ANALYSIS OF DATA

A. INTRODUCTION

An analysis of the previously presented data is presented in this section with the primary emphasis on the glass targets. Possible reasons or causes of the observed effects will be hypothesized and unanswered questions will be posed. A model for the laser-target interaction process for the glass target will be presented.

B. GLASS TARGET ANALYSIS

All of the glass target's data was analyzed for trends and possible explanations were noted. A list of general observations that occurred at all pressures will be presented with their possible causes. General observations for the high pressure range (1 - 0.1 atm), the medium pressure range (0.1 - 0.001 atm), and the low pressure range (below 0.001 atm) will also be presented with their possible causes.

1. General Trends at All Pressures

At the target's center, exfoliation occurred with approximately the same scale size throughout all of the pressures. It was also noted that Newton's rings as depicted in Figures 4.2 through 4.11 were present at all pressures. Utilizing the vaporization model developed in references four and five, the scale size would depend on

the glass temperature and the cooling rate. At all pressures, the center of the glass target must have reached the same maximum temperature and cooled at approximately the same rate. Also, with the aid of the vaporization model, the Newton's rings can be attributed to the interference pattern produced by the reflection of the light from the two surfaces of the horizontal cracks that developed in the glass (Figure 5.1).

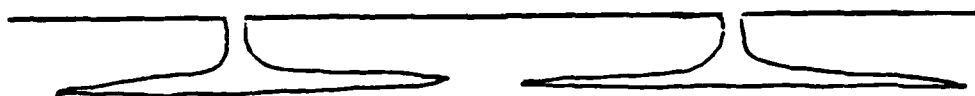


Figure 5.1 Model of Scales

Immediately outside of the area with the small scales, there was a region of larger scales. These larger scales tended to have cracks propagating in a radial direction (Figure 4.38 and 4.39). A possible cause for these larger scales is attributed to the lower maximum temperature of the glass in the target's perimeter area resulting from less energy deposition. In the burn pattern of Figure 3.7 and 3.8, clearly the maximum energy density occurred at the target's center and less energy was

deposited at the edge of the intensely damaged area. With a lower maximum temperature, the glass would develop larger scales, and the cracks would propagate radially outward from the area with the maximum temperature.

Long straight cracks were detected outside the area of maximum energy deposit at all pressures (Figure 4.43). These cracks were attributed to residual stresses that were introduced in the initial production of the glass. The crack formation and stress relief was initiated by the laser pulse.

The crater density was a function of the sizes of the craters (Figure 4.16 and 4.17). The larger the crater, the smaller the crater density. All attempts at correlating the crater size to the pressure dependence failed. The variation in crater size presumably is due to the fluctuation in the plasma parameters (T_e, λ_D, n_e, V_f) resulting in different arc burning times.

When ever a fern pattern as depicted in Figure 4.21 was observed, craters were not observed in that vicinity. At 1600X, these ferns appeared to be unipolar arcs that were propagating in a leap frog style. It is believed that this pattern is a result of a surface discharge.

As pictured in the burn patterns (Figures 3.7 and 3.8), the beam patterns have sides lobes and circular rings. These effects are attributed to the diffraction pattern of the laser's aperture. It was deduced that the

aperture was rectangular in shape with a rounded top and bottom; the unfocussed beam pattern verified this deduction.

2. General Trends at High Pressures

In the high pressure range (1 - 0.1 atm), there was intense crater damage at the target's center which dropped off linearly as the pressure decreased. The intense crater damage was a result of a large energy transfer. At high pressures, the plasma density in front of the target is greater and more energy is absorbed by the plasma with less energy reaching the target. The decrease in the plasma density is caused by the drop in the background gas pressure. The electric field in the sheath ($E = V_f / \lambda_D = (kT_e \cdot n)^{1/2}$) is responsible for the ignition of the unipolar arcs and the crater formation. If the plasma's electron temperature is proportional to the plasma density, then the electric field would be proportional to the plasma density. The linear drop in the crater density is thus attributed to a decrease in the electric field across the plasma sheath and a drop in the plasma density.

At the perimeter of the heavily damaged center area, craters were not observed outside the ring pattern which remained fixed around the exfoliation area. The ring appears to be caused by the melting of the glass which indicates an increase in the energy transfer in the ring location.

When the target was irradiated with the laser, a bright fluorescent-type flash was observed. It is surmised that the flash is a result of the ionization of the air.

3. General Trends in the Medium Pressure Range

In the medium pressure range (0.10 - 0.001 atm), the crater density at the target's center remained constant. This was attributed to the cut-off of the laser radiation that occurs with the formation of a critical density layer. This layer is formed when the plasma density equals the plasma's critical density. This critical density occurs when the laser's radian frequency equals the plasma frequency ($\omega^2 = \omega_p^2 = \{n_e \cdot e^2 / m_e \cdot \epsilon_0\}$). For the CO₂ laser (10.6 μm), this critical density equals $9.950 \times 10^{18} \text{ cm}^{-3}$. Once cut-off occurs, the parameters for the plasma (T_e, λ_D, n_e, V_f) between the surface and the critical density layer will remain approximately constant. This results in a constant crater density.

At the perimeter of the heavily damaged area, craters were present and their density remained constant throughout the medium pressure range. The presence of craters indicates the traverse propagation of the plasma at the target surface. The increased plasma density and the resulting plasma sheath resulted in unipolar arcing.

The surrounding ring that remained fixed in the high pressure range, shifted radially outward as the pressure was decreased. As the ring pattern shifted, as

many as three different rings were present and all rings exhibited the same wave-like quality (Figure 4.29). The ring pattern is attributed to the diffraction pattern of the laser's aperture. As the pressure decreased and the plasma cloud dispersed away from the target surface, the index of refraction of the plasma cloud, which is inversely proportional to the plasma density, increased resulting in the shifting of the energy deposition that caused the ring pattern. At the high pressures (1 - 0.1 atm), the plasma prevented damage to the target surface by the diffraction pattern; however as the plasma density decreased, the amount of energy that could penetrate to the surface increased resulting in the ring pattern.

The flash produced upon target illumination had a lower intensity than the high pressure range but still had the characteristics of a bright fluorescent-type flash.

4. General Trends in the Low Pressure Range

In the low pressure range (below 0.001 atm), the crater density at the target's center increased initially to a peak in the vicinity of 0.0005 atmospheres and then dropped off slightly to a constant crater density. The craters were more uniformly distributed than at atmospheric pressure. The decrease in the plasma shielding resulted in the piercing of the plasma by the laser radiation.

At the perimeter, there were larger crater sizes than at the center (compare Figures 4.7 and 4.15). It was

impossible to get an accurate size comparison; however, there are definitely larger craters at the perimeter. The plasma conditions allowed longer duration of arc burning resulting in larger crater size. More specifically, the higher electron temperature at the edge of the plasma cloud resulted in longer duration of arc burning.

The flash that occurred at target illumination was a dull incandescent-type flash. With less atmosphere to ionize, the flash's intensity would be smaller.

5. Summary of Trends and Possible Causes

The following is a summary of the general trends in each pressure region:

a. All Pressure Regions

- 1) Same size center scales.

Cause: Same maximum temperature and cooling rate.

- 2) Larger scales at damaged area's perimeter.

Cause: Lower maximum temperature.

- 3) Long straight cracks.

Cause: Residual stresses from production.

- 4) Crater size fluctuation.

Cause: Changes in the plasma parameters
(T_e, λ_D, n_e, V_f).

- 5) Fern pattern that occurs sporadically.

Cause: Surface discharge.

6) Side lobes and Rings.

Cause: Diffraction pattern of the laser's aperture.

b. General Trends at High Pressures

1) Linear drop in intense crater damage.

Cause: Increase in the Debye length and corresponding decrease in the sheath's electric field.

2) No perimeter craters.

Cause: Plasma sheath potential does not exceed the threshold of unipolar arcing.

3) Fixed ring pattern.

Cause: Laser aperture's diffraction pattern.

4) Bright fluorescent-type flash.

Cause: Ionization of air.

c. General Trends at Medium Pressures

1) Constant center crater density.

Cause: Constant plasma parameters between the surface and the critical density layer.

2) Perimeter craters appeared and their density remained constant.

Cause: The plasma expanded sideways over the target's surface and the plasma sheath's floating potential was large enough to support unipolar arcing.

- 3) The ring pattern shifted radially outward.

Cause: Changes in the plasma density resulting in a change of the index of refraction.

- 4) Reduced intensity of bright fluorescent-type flash.

Cause: Less atmosphere was available for ionization.

c. General Trends at Low Pressures

- 1) Center and perimeter crater density increased to a peak and then dropped off slightly to a constant density. The craters were uniformly distribution.

Cause: Decrease in plasma shielding resulting in piercing of the plasma by laser radiation.

- 2) Larger craters at the perimeter than at the center of the damaged area.

Cause: Longer arc burning time.

- 3) Dull incandescent-type flash.

Cause: Ionization of the thin atmosphere.

C. PLASTIC TARGET ANALYSIS

All of the plastic target's data was analyzed for trends and possible explanations were noted. A list of observations that occurred at all pressures will be presented with their possible causes, followed by the high pressure range (1 - 0.15 atm), the medium pressure range (0.15 - 0.0005 atm), and the low pressure range (below 0.0005 atm).

1. General Trends at all Pressures

At the target's center, there was massive melting at the laser beam's impact area, and conclusive evidence of a ring pattern was not observed at any pressure. The possible reason for the absence of the ring pattern is that the damaging threshold for the target surface was higher than for glass, therefore the energy deposition of the diffraction pattern was not large enough to cause damage.

2. General Trends at High Pressures

In the high pressure range (1 - 0.15 atm), there was intense melting at the target's center with very little splattering of material (Figure 4.65) outside the damaged area. The results indicate that the primary damage mechanism for the laser-target interaction was melting while the ambient pressure restricted the melted plastic to the damaged area.

At the perimeter of the heavily damaged area, craters were not observed. This indicates that the

plasma's floating potential did not exceed the threshold for unipolar arcing.

Upon target illumination, a bright fluorescent-type flash was observed. This is attributed to the ionization of the atmosphere.

3. General Trends at Medium Pressures

In the medium pressure range (0.15 - 0.0005 atm), perimeter craters occurred and their density increased to a maximum at 0.0005 atm. It is surmised that the increase of the floating potential for the outwardly expanding plasma resulted in the increase of unipolar arcing.

The crater size increased as the pressure was decreased. A possible cause for this is an increase in the floating potential resulting in longer burn times for the unipolar arcs.

Splattering of material outside of the target's damaged area occurred. With the decrease in ambient pressure, the melted material was able to expand further outside of the impact area.

A bright fluorescent-type flash occurred upon target illumination but with a lower intensity than the high pressure range. This is attributed to less atmosphere being available to ionize.

4. General Trends at Lower Pressures

The perimeter crater's density remained at approximately the same value at pressure below 0.0005

atmosphere. This indicates that the maximum floating potential across the sheath occurs at approximately 0.0005 atmosphere.

Splattering of melted material was more prevalent at lower pressures. As the ambient pressure was continually decreased, more melted material was able to expand further outside of the impact area.

A dull incandescent-type flash was observed upon target illumination in the low pressure range. The ionization of the thinly populated atmosphere caused the flash.

5. Summary of Trends and Possible Causes

a. All Pressure Regions

- 1) Massive melting occurred at the impact area.

Cause: Melting was the primary observable damage mechanism.

- 2) A ring pattern was not observed.

Cause: The energy deposition of the diffraction pattern was not large enough to cause damage.

b. General Trends at High Pressures

- 1) Craters were not observed at the perimeter.

Cause: The plasma sheath's potential was not large enough for unipolar arcing.

2) Bright fluorescent-type flash.

Cause: Ionization of the atmosphere.

c. General Trends at Medium Pressures

1) The perimeter crater density increased throughout the range to a maximum at 0.0005 atmospheres.

Cause: Increase of the plasma sheath's floating potential.

2) The crater density increased as the ambient pressure was decreased.

Cause: Longer arc burning.

3) Splattering of material outside damaged area.

Cause: Decreased pressure.

4) Bright fluorescent-type flash with less intensity than at higher pressures.

Cause: Less air to ionize.

4. General Trends at Lower Pressures

1) Perimeter crater density remained constant.

Cause: Maximum floating potential of plasma sheath.

2) Splattering of material outside damaged area was more prevalent.

Cause: Decreased pressure.

3) Dull incandescent-type flash.

Cause: Very little air to ionize.

D. LASER-GLASS INTERACTION MODEL (LGI)

The following model (LGI) is proposed to explain the previously listed characteristics of the laser-target interaction of soda lime glass. It serves to explain the observed effects in three ranges. The pressure ranges I, II, and III correspond to the high (1.0 - 0.1 atm), medium (0.1 - 0.001 atm), and low pressure ranges (below 0.001 atm). The primary emphasis in this model is the density profile of the laser induced plasma and the corresponding change in the index of refraction.

In pressure range I (1.0 - 0.1 atm), the background gas pressure is high, the relative kinetic temperature of the gas is low as compared to the plasma's temperature, and the expansion velocity of the plasma is small as compared to lower pressures. The two velocities of interest are the velocity parallel to the surface and the velocity normal to surface. As depicted by the arrows in Figure 5.1, the laser beam's energy profile consists of a main lobe assumed to be of a Gaussian nature and several hot spots resulting from the diffraction pattern of the laser's aperture. As the incident radiation strikes the surface, the following processes occur as described in chapter 2: desorption of surface gases, heating of the glass surface, plasma formation, ignition of the laser-supported-detonation wave, and cracking. The surrounding atmosphere interacts with the plasma restricting both the parallel and normal

velocities. In this pressure region, the plasma density is greater than the critical density ($\sim 10^{19} \text{ cm}^{-3}$), the plasma's index of refraction is much less than one, the plasma sheath remains close to the target surface, and the diffraction pattern outside of the heavily damaged area is absorbed by the plasma. The amount of energy not absorbed by the plasma does not exceed the threshold to initiate unipolar arcing at the target surface.

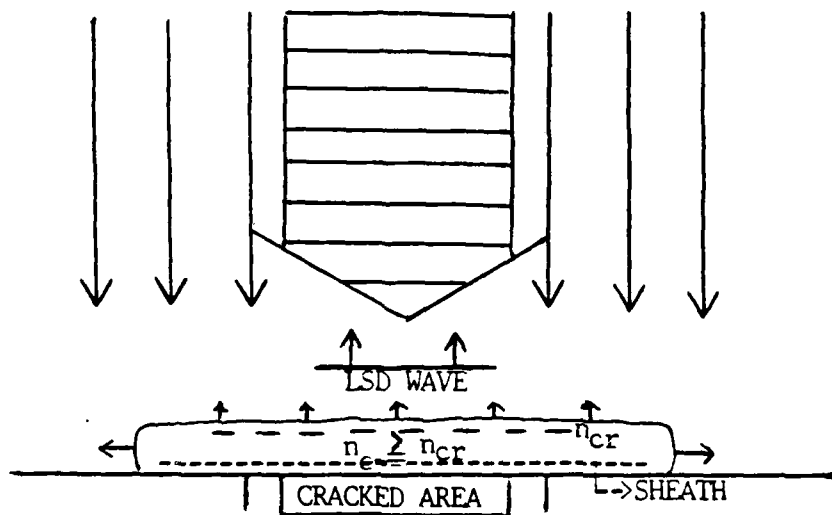


Figure 5.1 Pressure Range I of LGI Model

In pressure range II (0.1 - 0.001 atm) because of the decreased background pressure, there is more plasma expansion with larger velocities parallel and normal to the surface. The estimated plasma density ($\sim 10^{18} \text{ cm}^{-3}$), if the molecules are singularly ionized, and the critical density (10^{19} cm^{-3}) are almost equal, the plasma's index of refraction, which is inversely proportional to the density, is approximately equal to 0.5 and the plasma sheath width has increased. A Rayleigh-Taylor like instability resulting from the interaction of the expanding plasma with the background gas produces an erratic plasma density distribution, and the diffraction pattern is refracted away from the center of the damaged area. The combination of the plasma instability and the refraction causes the diffraction ring to shift radially outward from the target's center in a wave-like nature. The increased plasma expansion results in unipolar arcing outside of the heavily damaged area, and the decreased plasma density allows enough of the diffraction pattern's energy to melt the glass surface. (Figure 5.2)

In pressure range III (below 0.001 atm), the plasma expansion normal to the surface and parallel to the surface is maximum as is the velocities of the plasma in those respective directions. Because of this maximum expansion and being independent of the background gas pressure, the unipolar arcing crater density outside of the heavily

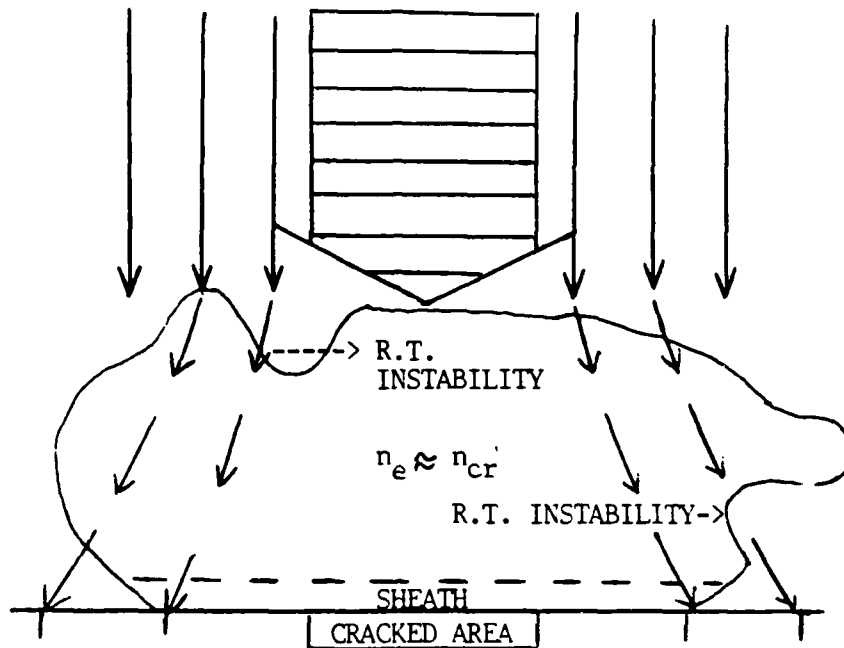


Figure 5.2 Pressure Range II of LGI Model

damaged area is constant, the plasma density is much less than the critical density, the index of refraction is approximately equal to one, the plasma sheath width remains constant, and the plasma density has decreased to the point that the transfer of the diffraction pattern's energy to the target surface can cause melting. (Figure 5.3)

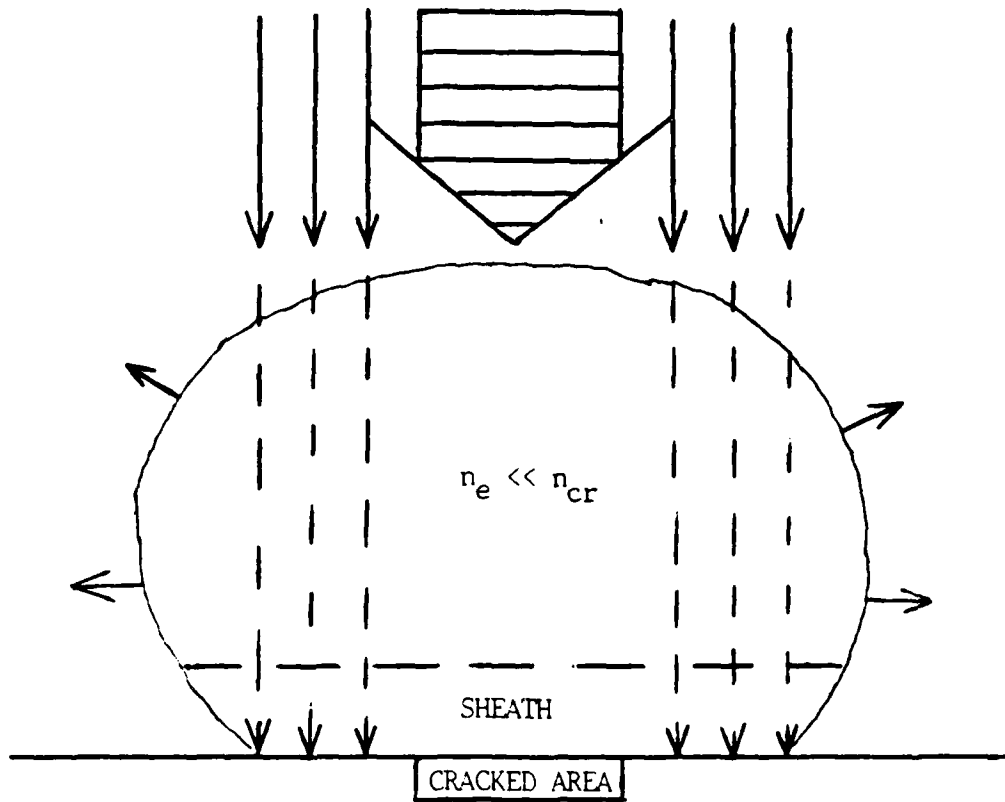


Figure 5.3 Pressure Range III of LIG Model

VI. CONCLUSIONS AND RECOMMENDATIONS

The primary purpose of this investigation was to determine the background gas pressure dependence of laser-induced unipolar arcing on the nonconducting materials of soda lime glass and plastic. Both types of targets were irradiated with the CO₂ laser with a power density of 5.25×10^6 W/cm² and a pulse width of 5.61 microseconds. For the glass targets, there was a linear drop in the unipolar arcing at the damaged area's center between the background pressures of one atmosphere and 0.1 atmosphere. Unipolar arcing outside the laser beam's impact area in this pressure range did not occur. Between the background pressures of 0.1 and 0.001 atmosphere, unipolar arcing at the damaged area's perimeter first occurred but remained constant. Unipolar arcing at the target's center remained constant in this pressure range. Below background pressures of 0.001 atmosphere, there was a sharp increase in both the perimeter and target center's unipolar arcing which peaked at approximately 0.0005 atmosphere and then dropped off slightly to a constant value. For the plastic targets, the intense damage at the laser beam's impact area prevented unipolar arcing analysis; however at the perimeter, the craters first appeared at 0.15 atmosphere and their density continued to increase as the background

pressure was decreased to 0.0005 atmosphere. It remained constant at lower pressures.

This investigation has studied the pressure dependence on soda lime glass and polystyrene. A model has been proposed to describe the laser-glass interactions; however, experimental verification and refinement is needed. An investigation into the mapping of the plasma expansion and plasma density near the target surface will help verify and refine the proposed model. Other nonconductive materials need to be examined to determine the unipolar arcing background pressure dependence, and the polystyrene targets need to be illuminated with a lower power density so as to determine the background pressure dependence of the center of the damaged area. The background pressure dependence of conducting materials needs to be examined and compared with the results of the nonconducting materials to further explore the nature of unipolar arcing and its importance at different background pressures. A list of future research projects can include the following topics.

1. Background pressure dependence on unipolar arcing of other nonconducting materials to include other types of glass.
2. Background pressure dependence on unipolar arcing on conducting materials.
3. Mapping of the plasma expansion and plasma density at the target's surface at different pressures.

4. Refinement of the laser-glass interaction model and its expansion to other materials.

It is strongly recommended that the study of the background pressure dependence on unipolar arcing be continued.

APPENDIX A

LUMONICS TE-822 HP CO₂ LASER OPERATING PROCEDURE

The CO₂ high energy pulsed laser is the primary research instrument for the study of plasma surface interactions at the Naval Postgraduate School. It must be operated in strict accordance with the operating procedures and safety precautions as established by prior research and updated in this appendix. [Refs. 3,4]

Prior to operating the laser system, an individual should complete a retina scan eye examination, receive an orientation briefing from the Physics Department's Lab Technician, and become thoroughly familiar with all procedural and safety aspects of the laser system.

During the orientation briefing, the potential hazards and safety requirements associated with the laser system should be stressed. The most detrimental hazard is the invisible CO₂ beam (10.6 microns) which is outside the visible range. Inadvertent exposure of the eyes and other body parts could result in injury; therefore, eye protection should be worn by all personnel, the target container confinement facility should be completely closed, and all interlocks should be operational before the laser is fired. **UNDER NO CIRCUMSTANCE** should an interlock be overridden unless the Physic Department's Lab Technician is

present or notified. The electrical interlocks, which are contained in the laser pulse initiation circuit, include:

A. Laser Enclosure Cover Interlocks(2) - ensures that the laser cabinet covers are in place to prevent electrical shock from the high voltage power supplies and other interior electrical components.

B. Laser Output Port Protective Cover Interlock - ensures that the laser is not inadvertently pulsed with the output port protective cover in place causing reflection back into the internal optics of the laser.

C. Cooling Water Flow - ensures that proper cooling water flow and pressure are maintained in the laser system so that the temperature sensitive high voltage power supplies do not overheat and fail on thermal overload. Thermal interlocks associated with the high voltage power supplies are designed to trip on temperatures in excess of 125 degrees Fahrenheit.

D. Laser Power Key - ensures that power is not available to the laser system until consciously applied by the operator.

E. Gas ON/OFF Switch - ensures that high voltage is not applied to the firing circuit unless gas flow has been properly established in the laser.

F. Plasma Laboratory Door - ensures that the laser firing circuit will be temporarily disabled if the laboratory door is opened during laser system operation. An audible alarm alerts operators of this problem.

Although the interlock system does afford considerable safety, electrical interlocks can never replace the requirement for an alert and conscientious operator. It is with this in mind that the following operational procedure is provided. The basis for the procedural sequence is contained within the Lumonics TE-822HP Instruction Manual [Ref. 14].

LASER SYSTEM START-UP is accomplished by following these sequential procedural steps:

1. Turn on the external voltage regulator and adjust its output for 119 volts.

NOTE

The high voltage power supplies inside the laser are NOT regulated; therefore, it is necessary to regulate the input voltage in order to acquire consistent laser output and performance characteristics.

2. Activate the laboratory door interlock by placing the toggle switch on the control box to the left of the door to the ON position.

3. Initiate cooling water flow and set the thermostat on the cooling unit to 15 degrees Celsius.

4. Set the Mode Select switch to SINGLE and the MULTIPLIER setting to X10.

NOTE

The MULTIPLIER control setting has three positions which are X.1, X1, and X10. These settings are used in

conjunction with the INTERNAL RATE potentiometer and apply their stated multiplication factors to establish a desired pulse repetition frequency. In the X1 and X10 positions the capacitors in the laser firing circuit are continuously charged, and the front panel voltmeter continuously registers the high voltage power supply voltage level. In SINGLE shot mode, repetitive pulsing is not possible but the X10 MULTIPLIER setting is used so that the high voltage power supply voltage can be monitored continuously during the conduct of the laser start up procedure.

5. Open the Helium, Carbon Dioxide and Nitrogen cylinder valves.

NOTE

The pressure regulators on each bottle are not adjustable until the gas is flowing through the laser system.

6. Turn the LASER POWER KEY to ON and note that the GAS OFF indicator is GREEN, the INTERLOCKS OPEN indicator is WHITE and the WARM UP INCOMPLETE indicator is YELLOW.

NOTE

The WARM UP INCOMPLETE indicator will extinguish after approximately 1 minute after the LASER POWER KEY is turned on.

7. Slowly open the HEAD EXHAUST VALVE by placing the valve operator in the vertical position. The valve is located in the lower right hand corner of the front control panel.

CAUTION

Failure to open the HEAD EXHAUST VALVE can cause the head to quickly become overpressurized. The laser is equipped with a NON-RESETTABLE 5 psig pressure relief valve which requires maintenance personnel to replace. Failure to open this relief valve will place the laser system out of commission until a replacement valve is installed. If there is excessive use of gas or if the laser energy is extremely erratic, notify the Physics Department Lab Technician, open the laser cabinet, and check for gas leaks; these are the signs of a blown head gasket.

8. Depress the GAS ON push button and observe the RED GAS ON indicator is lit while the GREEN GAS OFF indicator is extinguished.

9. After 15 seconds, adjust the pressure regulators to 10 psig.

10. Adjust the six Brooks flowmeters (three on the front control panel and three on the rear panel) to the following readings: 8 SCFH for N₂ and CO₂, and 6 SCFH for He.

NOTE

The gas flow rates have been established for Plasma research at the Naval Postgraduate School. These flow rates will produce single shot energies up to 15 joules with pulse widths of approximately 5 microseconds. These flow rates can be changed in accordance with the Lumonics Laser Instruction Manual.

NOTE

Continually monitor the pressure regulators and Brooks flowmeters throughout the operation of the laser to insure that the pulse width and energy output of the laser do not change. Fluctuation in the gas flow rate can change the pulse width and laser output significantly.

11. Remove the LASER OUTPUT PORT PROTECTIVE COVER.

CAUTION

Failure to remove the LASER OUTPUT PORT PROTECTIVE COVER could result in damage to the internal optics of the laser. There is an electrical interlock to prevent the firing of the laser with the cover in place; however, it should be physically verified that the cover or alignment mirror has been removed before firing.

12. Allow the gas to flow through the laser cabinet for 30 minutes before firing the laser.

NOTE

Do not stop the gas flow once it has been initiated except when a delay of more than 30 minutes will occur. The CO₂ will diffuse out of the molecular sieve inside the laser cavity thereby producing erratic energy shots.

13. Open the air cylinder and set the pressure regulator to 18 psig and establish a flow rate of 4 SCFH by adjusting the 6 flowmeters on the rear panel.

14. After the 30 minute warm up time is complete, prepare for an alignment check of the laser.

NOTE

Before every firing period, it is strongly recommended that the burn pattern and laser alignment are verified. Temperature changes, removal of laser cabinet covers, and earth quakes can shift the alignment of the laser.

15. Put a piece of black weighing paper on a brick, and place the brick at the alignment verification spot located inside the target containment area. Insure that the laser beam path is clear of all obstacles except the brick.

CAUTION

The target containment facility should have the door and windows closed at this point. NO ONE SHOULD BE INSIDE THE TARGET CONTAINMENT FACILITY. All personnel should always put eye protection on anytime the high voltage power supply is going to be activated.

16. Set the HV CONTROL KNOB fully counterclockwise to its MINIMUM setting and depress the RED HIGH VOLTAGE ON push button.

17. Turn the HV CONTROL KNOB clockwise until the voltmeter indicates 25 HV.

CAUTION

NEVER allow the high voltage to exceed 40 HV. The laser can operate at 40HV at a slow single pulse rate of one shot every minute; however, the laser designer recommends using the laser at settings of 36HV and below to avoid damage to the high voltage power supplies and internal optics.

18. The laser will now fire each time the SINGLE fire push button is depressed. Check to insure the chamber is clear and all personnel are wearing eye protection, and press the SINGLE fire push button.

19. Press the GREEN HIGH VOLTAGE OFF push button.

CAUTION

The GREEN HIGH VOLTAGE OFF push button should be illuminated before entering the target containment area to prevent accidental firing of the laser.

NOTE

The burn pattern for this laser is approximately a rectangle with dimensions 30mm by 33mm. If the burn pattern is not uniform, a cavity realignment will be necessary as described by the Lumonics Laser Instruction Manual. If the HV setting is 21 or below, the burn pattern will be nonuniform.

20. Place the alignment mirror on the laser output port, turn on the HeNe laser, and verify that the center of the damaged area on the weighing paper does in fact correspond to the alignment spot in the target containment facility. If the alignment is correct, the laser is prepared for research. If the alignment spot does not correspond to the center of the damaged area, either realign the laser as described in the Laser Instruction Manual or mark a new spot if the alignment is close.

21. While using the HeNe laser to align the optical components of the system, align the beam splitter and the energy meter probe. Place a brick in the reflection line of site as a dump for the CO₂ laser.

WARNING

All optics and detector surfaces should be free of dust. Use canned gas to remove the dust.

22. Remove the alignment mirror, close the target containment facility, and put on eye protection. Push the RED HIGH VOLTAGE ON push button, push the SINGLE fire push button, and observe the energy meter reading.

23. Adjust the HV CONTROL KNOB setting on the front panel to the desire energy output.

NOTE

Verify the energy output of the laser before irradiating targets if more than 5 minutes has elapsed since the previous firing. This verification will reduce the amount of fluctuation inevitable with a CO₂ laser.

LASER SYSTEM SHUT DOWN procedures are as follows:

1. Insure that the GREEN HIGH VOLTAGE OFF push button is illuminated.
2. Close all of the gas tanks.
3. Wait until all SCFH meters are reading zero, and then push the GAS OFF push button.
4. Close the HEAD EXHAUST VALVE.
5. Turn the LASER POWER KEY to OFF.

WARNING

Before turning off the cooling unit, the HEAT light must be illuminated. If necessary increase the temperature of the cooling unit until the HEAT light illuminates.

6. Turn off the cooling unit.
7. Cover the LASER OUTPUT PORT.
8. Turn off the door interlock switch and the audible alarm switch.
9. Cover the laser with the electric blanket and turn the blanket on the setting of 6.

NOTE

It is only necessary to turn on the electric blanket to maintain the optics of the laser at a constant temperature. If the laser is not going to be in use for several days, then temperature control of the optics is not required.

10. If the laser is not going to be utilized for several days, turn off the external voltage regulator.

APPENDIX B

VEECO 400 VACUUM SYSTEM OPERATING PROCEDURES

The VEECO 400 Vacuum system is utilized in conjunction with the CO₂ laser for research of plasma surface interactions. Targets can be irradiated with the CO₂ laser in reduced pressure conditions ranging from 760 torr to 10⁻⁶ torr. This system must be operated in strict accordance with the updated operating procedures as established in this appendix [Ref. 18].

Prior to operating the vacuum system, an individual should receive an orientation briefing from the Physics Department's Lab Technician and become thoroughly familiar with all procedural and safety aspects of the vacuum system.

During the orientation briefing, the potential hazards and safety requirements associated with the vacuum system should be stressed. The most significant of these hazards are the exhaust fumes that can develop if the exhaust system fails and the electrical danger created if the cooling hose breaks. Upon detection of any unusual odors, leaks or sounds, the Physics Department's Lab Technician should be immediately notified. It is with this in mind that the following operational procedure is provided.

VACUUM SYSTEM START-UP is accomplished by following these sequential procedural steps:

NOTE

Figure B.1 depicts the position of the controls on the VEECO vacuum system referenced in the following instructions.

NOTE

CLOCKWISE rotation of the vents or valves CLOSES them. COUNTER-CLOCKWISE rotation opens the valves.

WARNING

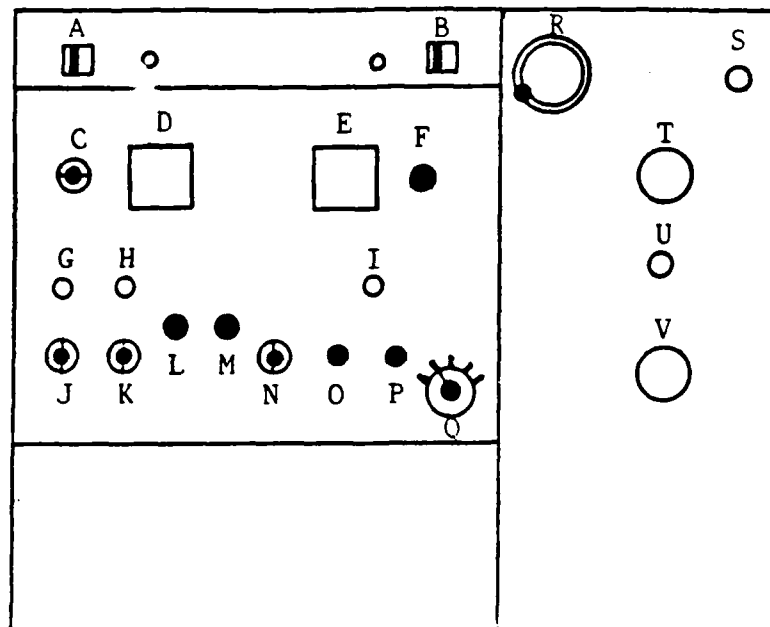
When ever any valve is opened, rotate the control counter-clockwise SLOWLY to avoid damaging the vacuum system.

1. Close all valves and vents.
2. Set the PRESSURE MULTIPLIER KNOB to 10^{-4} position.
3. Turn on the MECHANICAL PUMP ON/OFF SWITCH. Let the mechanical pump run for approximately 30 minutes to outgas the oil reservoir.

NOTE

The time to outgas the oil reservoir will depend on how long the pump has been off.

4. Open the FORELINE VALVE to allow the diffusion pump oil to be outgassed.
5. Turn on the vacuum gauge using the POWER ON/OFF SWITCH. The POWER ON BULB should illuminate.
6. Set the TC-1/TC-2 THERMOCOUPLE SWITCH to the TC-1 position.



- A - MECHANICAL PUMP ON/OFF SWITCH
- B - DIFFUSION PUMP ON/OFF SWITCH
- C - TC-1/TC-2 THERMOCOUPLE SWITCH
- D - THERMOCOUPLE GAUGE
- E - IONIZATION GAUGE
- F - ZERO ADJUSTMENT
- G - POWER ON BULB
- H - DEGAS ON BULB
- I - FILAMENT ON BULB
- J - POWER ON/OFF SWITCH
- K - DEGAS ON/OFF SWITCH
- L - CURRENT SET KNOB
- M - CURRENT ADJUST KNOB
- N - READ CURRENT SWITCH
- O - FILAMENT CURRENT OFF PUSH BUTTON
- P - FILAMENT CURRENT ON PUSH BUTTON
- Q - PRESSURE MULTIPLIER VALVE
- R - HIGH VACUUM VALVE
- S - CHAMBER VENT
- T - ROUGHING VALVE
- U - MECHANICAL PUMP VENT
- V - FORELINE VALVE

Figure B.1 VEECO VACUUM CHAMBER CONTROLS

NOTE

TC-1 allows observation of the pressure in the foreline subsystem of the vacuum system. TC-2 allows observation of the pressure of the chamber.

7. Turn on the cooling tap water.

WARNING

If the diffusion pump on/off switch is turned on without the flow of the cooling water, the diffusion oil overheats and evaporates causing the heating coil to burn out.

8. When the thermocouple gauge gets below 20 microns, turn on the DIFFUSION PUMP ON/OFF SWITCH.

NOTE

As the diffusion oil heats, the pressure on the thermocouple gauge will increase initially, and then begin decreasing again. The diffusion pump is wired to a flow switch on the cooling water line. The flow switch will turn off the diffusion pump if there is a loss of cooling water flow.

9. Add liquid nitrogen to the cold trap.
10. After 20 minutes, turn on the ion gauge by pressing the FILAMENT CURRENT ON push button. The FILAMENT ON BULB should illuminate.

HIGH VACUUM CHAMBER OPERATION is accomplished by following these sequential procedural steps:

1. Close the FORELINE VALVE.
2. Switch the TC-1/TC-2 THERMOCOUPLE SWITCH to the TC-2 position.

3. Open the ROUGHING VALVE.

WARNING

In the following step, be sure that the IONIZATION GAUGE does not go off scale.

4. When the THERMOCOUPLE GAUGE reads below 50 microns, CLOSE the ROUGHING VALVE, and OPEN the FORELINE VALVE. SLOWLY open the HIGH VACUUM VALVE.

5. When the IONIZATION GAUGE gets below 0.2×10^{-4} torr, switch the PRESSURE MULTIPLIER KNOB to 10^{-5} torr.

6. After the pressure gets below 5×10^{-5} torr, switch up the READ CURRENT SWITCH to read the emission current. It should read 10ma; if not, adjust it using the CURRENT ADJUST KNOB and CURRENT SET KNOB.

NOTE

It will probably be necessary to outgas the ion tube for approximately 15 minutes in order to read higher vacuum.

7. Turn on the DEGAS ON/OFF SWITCH. The filament may trip, and the FILAMENT ON BULB may extinguish. Wait 1 minute and push the FILAMENT CURRENT ON push button again. If the filament bulb extinguishes again, wait five minutes and try again.

8. When the IONIZATION GAUGE reaches $.2 \times 10^{-5}$ torr, switch the PRESSURE MULTIPLIER KNOB to 10^{-6} torr.

OPENING THE CHAMBER is accomplished by following these sequential steps:

1. Set the PRESSURE MULTIPLIER KNOB to 10^{-4} setting.

2. CLOSE the HIGH VACUUM VALVE.

3. SLOWLY open the CHAMBER VENT. After the air has stopped flowing into the chamber, it can be opened.

SYSTEM IDLING CONDITION (for temporary storage with the vacuum system still operating) is accomplished by following these sequential steps.

1. Complete the HIGH VACUUM CHAMBER OPERATIONS to evacuated the chamber.

2. Close the HIGH VACUUM VALVE.

3. Press the FILAMENT CURRENT OFF push button.

NOTE

The vacuum system can operate in this configuration for several days until the next experiment is conducted.

TO SHUT DOWN THE SYSTEM COMPLETELY, complete the following sequential steps:

1. Press the FILAMENT CURRENT OFF push button.

2. Close the HIGH VACUUM VALVE and the ROUGHING VALVE.

3. Turn off the DIFFUSION PUMP SWITCH.

WARNING

Let the diffusion pump cool down for at least 30 minutes to avoid damaging the pump before proceeding with these procedures.

4. Close the FORELINE VALVE.

5. Turn off the cooling water.

6. The mechanical pump can be left running in this position indefinitely. To secure the mechanical pump, turn

off the MECHANICAL PUMP ON/OFF SWITCH and open the MECHANICAL PUMP VENT for approximately 5 minutes. When the air flow has stopped, close the MECHANICAL PUMP VENT.

LIST OF REFERENCES

1. American Physics Society, "The Science and Technology of Directed Energy Weapons", Reviews of Modern Physics, v. 59, July 1987.
2. Schwirzke, F., Unipolar Arcing, A Basic Laser Damage Mechanism, Report NPS-61-83-008, Naval Postgraduate School, Monterey, California, 5 May 1983.
3. Olson, J., CO₂ Pulsed Laser Damage Mechanisms and Assessment of Plasma Effects (Unfocussed Beam), M.S. Thesis, Naval Postgraduate School, Monterey, California, December 1986.
4. G. A. Simons and M. G. Miller, Glass Hardening to Laser Radiation, Report PSI-TR-400, Army Materials and Mechanics Research Center, Watertown, Maryland, May 1984.
5. G. A. Simons, P. K. S. Wu, and M. G. Miller, The Optimization of Glass Parameters for Hardening Against Out-of-Band Laser Radiation, Report PSI-TR-682, Army Materials and Mechanics Research, Watertown, Maryland, August 1987.
6. Weston, R. L., CO₂ Pulsed Laser Damage Mechanisms and Assessment of Plasma Effects (Focussed Beam), M.S. Thesis, Naval Postgraduate School, Monterey, California, December 1986.
7. Nielsen, P. E. and Canavan, G. H., "Theory of Laser-Target Interaction", Journal of Defense Research, v. 7B, pp.439-446, May 1975.
8. Naval Research Laboratory Report 7728, Response of Materials to Laser Radiation: A Short Course, by J. T. Schriempf, July 1974.
9. Byron, S. and Klosterman, E. L., "Laser-Supported Absorption Waves", Journal of Defense Research, v. 7B, pp. 468-481, May 1975.
10. Naval Postgraduate School Report NPS-61Nb-75121, Laser Effects Handbook 3 Laser Absorption Wave Phenomena, by D. E. Harrison, December 1975.

11. Robson, A. E. and Thonemann, P. C., "An Arc Maintained on an Isolated Metal Plate Exposed to a Plasma", Proceedings of the Physical Society of London, v. 73, pp. 508-512, March 1959.
12. Schwirzke, F., "Laser Induced Unipolar Arcing", Laser Interaction and Related Plasma Phenomena, v. 6, pp. 335-352, 1984.
13. Schwirzke, F. and Taylor, R. J., "Surface Damage by Sheath Effects and Unipolar Arcs", Journal of Nuclear Materials, v. 93 and 94, pp. 780-784, 1980.
14. Lumonics Inc., Instruction Manual, Lumonics TE 820 HP Series CO₂ Lasers, 1976.
15. Matheson Gas Products, Inc., Matheson Gas Products Catalog 88, pp. 180, 1988.
16. Hecht, E., Optics, 2nd ed., pp. 226-228, Addison-Wiley Inc., 1987.
17. Holland, L., Vacuum Deposition of Thin Films, Cox and Wyman Limited, 1970
18. Wilson, C. E., Laser Damage Facility, M.S. Thesis, Naval Postgraduate School, Monterey, California, December 1985.

INITIAL DISTRIBUTION LIST

	No. Copies
1. Defense Technical Information Center Cameron Station Alexandria, Virginia 22304-6145	2
2. Library Code 0142 Naval Postgraduate School Monterey, California 93943-5002	2
3. Office of Naval Research Attn: Dr. R. Pohanka 800 N Quincy Street Arlington, Virginia 22217	1
4. Naval Research Laboratory Attn: Dr. T. Wieting Washington, DC 20375	1
5. Professor F. R. Schwirzke, Code 61Sw Department of Physics Naval Postgraduate School Monterey, California 93943-5000	2
6. Professor K. E. Woehler, Code 61Wh Department of Physics Naval Postgraduate School Monterey, California 93943-5000	1
7. Robert Sanders, Physical Scientist, Code 61 Department of Physics Naval Postgraduate School Monterey, California 93943-5000	1
8. Professor S. L. Garrett, Code 61Gx Department of Physics Naval Postgraduate School Monterey, California 93943-5000	1
9. Physical Sciences Inc. Attn: Dr. G. A. Simons Research Park, P.O. BOX 3100 Andover, Maryland 01810-7100	1
10. Captain Adam R. Wojtowich USMA Physics Department West Point, New York 10996	2